Ozone pollution around a coastal region of South China Sea: interaction between marine and continental air

Hao Wang[1,*], **Xiaopu Lyu**[1,*], **Hai Guo**[1], **Yu Wang**[1], **Shichun Zou**[2], **Zhenhao Ling**[3], **Xinming Wang**[4], **Fei Jiang**[5], **Yangzong Zeren**[1], **Wenzhuo Pan**[1], **Xiaobo Huang**[6], **and Jin Shen**[7]

[1]Air Quality Studies, Department of Civil and Environmental Engineering, Hong Kong Polytechnic University, Hong Kong, China
[2]School of Marine Sciences, Sun Yat-sen University, Guangzhou, China
[3]School of Atmospheric Sciences, Sun Yat-sen University, Guangzhou, China
[4]Guangzhou Institute of Geochemistry, Chinese Academy of Sciences, Guangzhou, China
[5]International Institute for Earth System Science, Nanjing University, Nanjing, China
[6]Shenzhen Academy of Environmental Sciences, Shenzhen, China
[7]State Key Laboratory of Regional Air Quality Monitoring, Guangdong Key Laboratory of Secondary Air Pollution Research, Guangdong Environmental Monitoring Center, Guangzhou, China
[*]These authors contributed equally to this work.

Correspondence: Hai Guo (ceguohai@polyu.edu.hk) and Fei Jiang (jiangf@nju.edu.cn)

Abstract. Marine atmosphere is usually considered to be a clean environment, but this study indicates that the near-coast waters of the South China Sea (SCS) suffer from even worse air quality than coastal cities. The analyses were based on concurrent field measurements of target air pollutants and meteorological parameters conducted at a suburban site (Tung Chung, TC) and a nearby marine site (Wan Shan, WS) from August to November 2013. The observations showed that the levels of primary air pollutants were significantly lower at WS than those at TC, while the ozone (O_3) value was greater at WS. Higher O_3 levels at WS were attributed to the weaker NO titration and higher O_3 production rate because of stronger oxidative capacity of the atmosphere. However, O_3 episodes were concurrently observed at both sites under certain meteorological conditions, such as tropical cyclones, continental anticyclones and sea–land breezes (SLBs). Driven by these synoptic systems and mesoscale recirculations, the interaction between continental and marine air masses profoundly changed the atmospheric composition and subsequently influenced the formation and redistribution of O_3 in the coastal areas. When continental air intruded into marine atmosphere, the O_3 pollution was magnified over the SCS, and the elevated O_3 (> 100 ppbv) could overspread the sea boundary layer ~ 8 times the area of Hong Kong. In some cases, the exaggerated O_3 pollution over the SCS was recirculated to the coastal inshore by sea breeze, leading to aggravated O_3 pollution in coastal cities. The findings are applicable to similar mesoscale environments around the world where the maritime atmosphere is potentially influenced by severe continental air pollution.

1 Introduction

Ozone (O_3) plays a central role in photochemical oxidation processes in the troposphere via direct reaction, photolysis and the subsequent reactions to produce the hydroxyl radical (Monks et al., 2015; Seinfeld and Pandis, 2016). As a strong oxidant, O_3 at surface level is recognized to be a threat to human health (WHO, 2003; Bell et al., 2007) and has a detrimental impact on vegetation (Fowler et al., 2009) and infrastructure (Kumar and Imam, 2013). Tropospheric O_3 is also the third most important greenhouse gas (IPCC, 2014) and is referred to a short-lived climate pollutant (Shindell et al., 2012).

To mitigate O$_3$ pollution in the troposphere, tremendous efforts from both scientific and regulatory communities have been made in the past three decades (NRC, 1991; NARSTO, 2000; Monks et al., 2015). The O$_3$ levels started to decrease at many locations, such as Jungfraujoch in Switzerland, Zugspitze in Germany, Mace Head in Ireland and parts of California and the eastern US (Lefohn et al., 2010; Cui et al., 2011; Parrish et al., 2012; Derwent et al., 2013; Lin et al., 2017). However, increasing studies showed that surface O$_3$ was elevated rapidly in East Asia in the last decade (Ding et al., 2008; Xu et al., 2008; Parrish et al., 2012; Xue et al., 2014; Zhang et al., 2014; Sun et al., 2016; Lin et al., 2017; Wang et al., 2017). For example, the observational data revealed that regional O$_3$ concentrations increased at a rate of 0.86 ppbv yr^{-1} in Pearl River Delta (PRD) from 2006 to 2011 (Li et al., 2014), at a rate of 0.56 ppbv yr^{-1} in Hong Kong from 2005 to 2014 (Wang et al., 2017), and even at a rate of 1.7–2.1 ppbv yr^{-1} (summertime only) at Mount Tai in central eastern China (Sun et al., 2016).

Hong Kong and the adjacent PRD are the most industrialized regions along the coast of South China Sea (SCS), and they suffer from serious O$_3$ pollution (Zheng et al., 2010; Guo et al., 2013; Ling et al., 2013). Numerous studies demonstrated that in addition to long-range transport (Chan, 2002; Guo et al., 2009; Wang et al., 2009) and local photochemical production (Ding et al., 2013b), tropical cyclones and mesoscale circulations are conducive to the occurrence of high-O$_3$ events (Yin, 2004; Huang et al., 2005; Yang et al., 2012; Jiang et al., 2015; Wei et al., 2016). In a number of studies, the tropical cyclone has been considered as the most conducive driver to the occurrence of O$_3$ episodes in Hong Kong (Yin, 2004; Ling et al., 2013) because it generally causes peripheral subsidence, stagnation air and inversion layers, which favor the production and accumulation of O$_3$.

Mesoscale circulations (e.g., sea–land breezes (SLBs) and mountain–valley breezes) also play important roles in O$_3$ distribution and transport in the coastal cities like Hong Kong with complex topography and land cover (Liu and Chan, 2002; Ding et al., 2004; Lu et al., 2010; Guo et al., 2013). For instance, Guo et al. (2013) demonstrated that upslope winds brought pollutants including O$_3$ from low-lying areas to the peak of Mt. Tai Mo Shan (957 m a.s.l.) in Hong Kong. Ding et al. (2004) simulated a multi-day SLB-related O$_3$ episode and discussed the influence of SLB circulation on the transport of oxidant precursors, the residence time and re-entry of photochemical compounds. Lu et al. (2010) simulated the SLB in the 2003/2004 winter and revealed that the urbanization of Shenzhen might significantly enhance the sea breeze to the west of Hong Kong in the early afternoon, which worsened the local air pollution.

Both coastal human activities and marine atmospheric cyclic behavior can significantly affect the air pollution level in coastal urban environments (Adame et al., 2010; Velchev et al., 2011). Exploring SLBs provides an important way to understand the interaction between continental air and marine atmosphere, which has long been a focus of coastal air quality, global tropospheric chemistry and climate change research. Surprisingly, few studies investigated SLBs in Hong Kong although about 70 SLB days per year on average were observed in Hong Kong and the PRD region (Zhang and Zhang, 1997). Therefore, the association between mesoscale recirculation and air pollutants over the SCS and subtropical continental region is still not well established, which seriously limits our understanding of the interplay of continental and marine air masses in this region. Furthermore, previous O$_3$ studies carried out in this region neither paid enough attention to the variations of volatile organic compounds (VOCs, one important group of O$_3$ precursors) nor established any field measurements on an island, an ideal site for observation of marine air mass with less interference from local emissions, for understanding the O$_3$ pollution around the coastal region of the SCS (Parrish et al., 1998). So far, only a handful of studies intensely evaluated the chemical characteristics of air masses under various synoptic systems (Wang et al., 2005; Guo et al., 2009, 2013; Li et al., 2018).

This study aims to comprehensively characterize interaction between continental anthropogenic emissions and marine atmosphere over a coastal region of the SCS by concurrent measurements and in-depth analysis of air pollutants at a marine site over the SCS and a suburban site in Hong Kong. Firstly, the spatial and temporal variations of measurements are described to give an overall picture of the campaign as well as to directly evaluate how continental outflows polluted the marine atmosphere over the SCS. After that, the chemical and meteorological characteristics of air masses associated with high O$_3$ concentrations are explored. Finally, the interplay between the maritime and continental air masses and its influence on regional air quality are discussed.

2 Methodology

2.1 Sampling sites

Field measurements were carried out concurrently at a suburban site and a marine site over SCS (Fig. 1). The suburban Tung Chung (TC; 22.29° N, 113.94° E) site, part of the Hong Kong Environmental Protection Department (HKEPD) air quality monitoring network, is located in southwestern Hong Kong, about 3 km south of the Hong Kong International Airport at Chek Lap Kok with Hong Kong's urban center about 20 km to the southwest and Macau 38 km to the northeast. It is a newly developed residential town adjacent to the busy highway and railway lines. The sampling instruments were installed on the rooftop of a building with a height of 27.5 m a.s.l. A more detailed description of the TC site can be found in our previous publications (Cheng et al., 2010b; Jiang et al., 2010).

The marine site, Wan Shan island (WS; $21.93°$ N, $113.73°$ E), is located 40 km southeast of Zhuhai and is bounded to the north by the Pearl River Estuary, with a straight distance of about 44 km to TC. WS has an area of 8.1 km^2 and a population of about 3000 with sparse anthropogenic emissions at the island. The isolated island features a subtropical maritime climate. The measurement site was set up on the rooftop of the National Marine Environmental Monitoring Station with a height of about 65 m a.s.l.

High-O$_3$ mixing ratios are frequently observed in Hong Kong in late summer and autumn (Ling et al., 2013) when tropical cyclones and the northeast monsoon prevail, respectively. During this period, WS is right in the downwind direction of TC, which facilitates the study of the interaction between the inland pollution and the marine environment.

2.2 Measurement techniques

2.2.1 Measurements of trace gases and meteorological parameters

The sampling campaign was conducted from 10 August to 21 November across late summer and autumn in 2013. At WS, trace gases (i.e., NO$_x$, O$_3$, SO$_2$ and CO) were continuously monitored with a time resolution of 1 min. NO-NO$_2$-NO$_x$ was measured using a heated molybdenum NO$_2$-to-NO converter and a chemiluminescence analyzer (Thermo Environmental Instruments (TEI), model 42i) with a range of 0–200 ppbv and a lower detection limit of 0.40 ppbv. It was noteworthy that the measured NO$_x$ might include other oxidized reactive nitrogen that was converted by the molybdenum. Thus, the NO$_x$ concentrations given below were considered the upper limits of their actual values (Dunlea et al., 2007; Ran et al., 2011). O$_3$ was monitored with a commercial UV photometric analyzer (TEI, model 49i) with a range of 0–0.050 to 200 ppm and a lower detection limit of 1.0 ppbv. SO$_2$ was measured using a pulsed UV fluorescence approach (TEI, model 43S). CO was measured by a non-dispersive infrared analyzer based on gas filter correlation technology (API, model 300). Quality assurance and control procedures (e.g., instrumental maintenance and calibration) for these devices have been described elsewhere (Guo et al., 2009, 2013). Meteorological parameters, including temperature, relative humidity, solar radiation, wind speed and wind direction, were routinely monitored by a weather station (Vantage Pro 2 plus, Davis Instruments) with a time resolution of 5 min. At TC, hourly data of the aforementioned trace gases and meteorological parameters were obtained from the HKEPD (http://epic.epd.gov.hk/ca/uid/airdata). Detailed information of the quality assurance and control protocols is available in the HKEPD report (HKEPD, 2015).

2.2.2 Sampling and analysis of VOCs

Concurrent VOC samples (i.e., non-methane hydrocarbons (NMHCs) and carbonyls) were collected on 21 selected days (including both non-O$_3$ episodes and O$_3$ episodes) at both sites. These days were selected on the basis of weather prediction and meteorological data analysis for potentially high- and low-O$_3$ days. An O$_3$ episode day is the day when the peak 1 h averaged O$_3$ mixing ratio exceeds 100 ppbv (Level II of China National Ambient Air Quality Standard). Please refer to our previous publication for details of this method (Guo et al., 2009).

The whole-air samples of NMHCs were collected using 2 L electro-polished stainless steel canisters. The canisters were cleaned, conditioned and evacuated before being used for sampling. A metal bellows pump was used to fill up the canisters with sample air over 1-hour integration (with a flow restrictor) to a pressure of 40 psi. Seven 1-hour VOC samples (every 2 h during 07:00–19:00 inclusive) were collected simultaneously at each site. Intensive VOC sampling was also carried out at WS on 7 selected days (i.e., 3, 4, 9 and 22–25 October) with 11 1-hour samples (every 2 h during 01:00–22:00 inclusive). Totally, 311 valid VOC samples (144 at TC and 167 at WS) were collected in addition to about 5 % field blanks and 5 % parallel samples for quality assurance purpose. The speciation and abundance of 59 C$_2$–C$_{11}$ NMHCs in the canisters were determined by a preconcentrator (model 7100, Entech Instruments Inc., California, USA) coupled with an Agilent 5973N gas chromatography–mass selective detector–flame ionization detector (GC-MSD-FID, Agilent Technologies, USA). The detection limit of NMHCs was 3 pptv with a measurement precision of 2–5 % and a measurement accuracy of 5 %. Detailed information of the analysis system and quality control and quality assurance for VOC samples can be found elsewhere (Simpson et al., 2010).

Carbonyl samples were collected using silica-gel-filled cartridges impregnated with acidified 2,4-dinitrophenylhydrazine (DNPH). Air samples were drawn through the cartridge at a flow rate of 0.4–0.6 L min^{-1} for 2 h; the flow rate through the cartridges was monitored with a rotameter which was calibrated before and after each sampling. An O$_3$ scrubber was connected to the inlet of the DNPH–silica gel cartridge to prevent interference from O$_3$. In total, 227 carbonyl samples (124 at TC and 103 at WS) were collected with 5 and 6 samples per non-O$_3$ and O$_3$ episode day (every 2 h during 07:00–18:00 inclusive), respectively. All cartridges were stored in a refrigerator at 4 °C after sampling. The sampled carbonyl cartridges were eluted slowly with < 5 mL of acetonitrile in the direction opposite to sampling flow into a 5 mL brown volumetric flask, followed by adding acetonitrile to a constant volume of 5 mL. A 20 µL aliquot was injected into the high performance liquid chromatography (HPLC) system through an autosampler. The operating conditions of the HPLC are shown in Table S1 in the Supplement. Typically, C$_1$–C$_9$
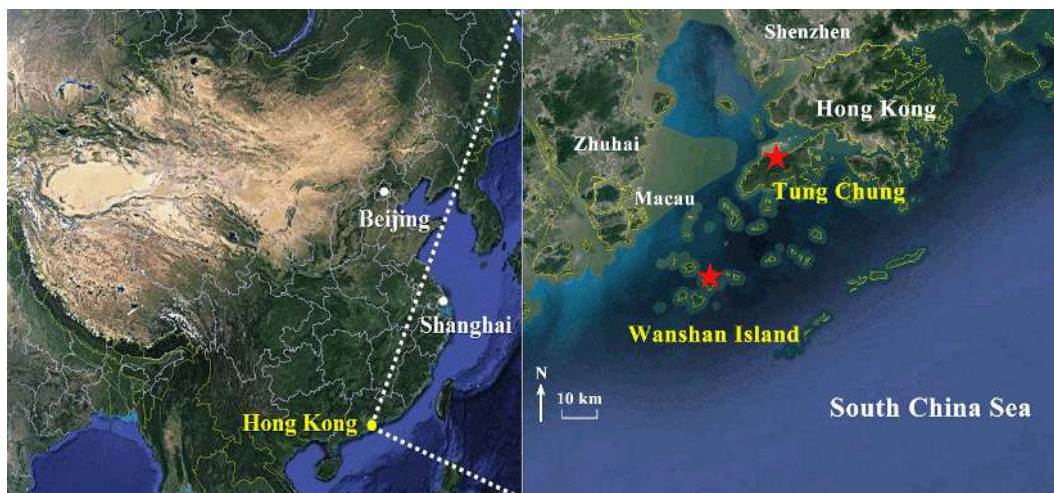
Figure 1. Locations of the sampling sites (red stars) and the surrounding environment.

carbonyl compounds were measured efficiently with a detection limit of ~ 0.2 ppbv.

2.3 Observation-based model

A photochemical box model coupled with the Master Chemical Mechanism v3.2 (PBM-MCM) was applied to simulate the O_3 production at WS and TC for the VOC sampling days. The PBM-MCM model is a zero-dimensional photochemical box model combined with a near-explicit chemical mechanism consisting of 5900 species and 16 500 reactions, which fully describes the mechanisms of homogeneous reactions in the atmosphere (Jenkin et al., 1997, 2003; Saunders et al., 2003). The simulation was constrained by hourly data of meteorological parameters (i.e., temperature and relative humidity) and air pollutants (NO, NO_2, CO, SO_2 and 51 measured VOCs). Since the sampling interval was 2 h for each sample, cubic spline interpolation was used to derive VOC concentrations at each hour for modeling purpose. Please see our previous publication for details (Wang et al., 2017). HONO has been recognized as an important source of OH, influencing O_3 formation significantly (Kleffmann, 2007). Since we did not measure HONO mixing ratios in this study, the average diurnal profiles of HONO observed at TC in autumn 2011 (Xu et al., 2015) and at a coastal background site (Hok Tsui, HT) in southeast Hong Kong in autumn 2012 (Zha, 2015) were applied to the photochemical simulations at TC and WS, respectively. Figure S1 in the Supplement shows the average diurnal cycles of HONO at TC and HT. The use of the aforementioned diurnal profiles might increase the uncertainty of model simulation. However, we believe that the newly introduced uncertainties could not be too high, because HONO observations at TC and HT were carried out 2 years and 1 year before the sampling campaign of this study, respectively. In addition, HT was comparable to WS in aspects of local emissions (nearly free of anthropogenic

emissions), air mass category (mixed continental and marine air) and location (to the south of Hong Kong and on the SCS). It is noteworthy that the atmospheric physical processes (i.e., vertical and horizontal transport) were not considered in this model. In addition, the inherent uncertainty of NO_x measurement mentioned above might slightly affect the modeling results. The PBM-MCM model has been successfully applied in previous studies (Cheng et al., 2010a; Lam et al., 2013; Ling et al., 2014). Details of the model construction can be found in Saunders et al. (2003) and Lam et al. (2013).

2.4 WRF-CMAQ simulation and backward particle release model

In this study, the Weather Research and Forecasting (WRF v3.7.1) model (Skamarock et al., 2008) was used to simulate vertical and horizontal wind fields for various weather systems observed in this campaign and then provided meteorological parameters required by US EPA Community Multiscale Air Quality (CMAQ v4.7.1) model (www.epa.gov/cmaq). CMAQ is a three-dimensional Eulerian atmospheric chemistry and transport modeling system, which includes complex physical and chemical processes, such as physical transport and diffuse, gas and aqueous chemical transformation, and so on; it can treat multiple pollutants simultaneously from local to continental scales. A domain system composed of four nested grids (81, 27, 9, 3 km) was adopted to better suit the simulation of mesoscale weather systems, as shown in Fig. S2. The domain with finest resolution (3 km) covers the Pearl River Estuary region. Vertically, there were 31 sigma levels for all domains, with the model top fixed at 50 hPa. The major selected physical schemes invoked in WRF and chemical mechanisms used in CMAQ are shown in Table S2. The input meteorological data were made using NCEP FNL (final) data with a horizontal resolution of $1° \times 1°$ (https://rda.ucar.edu/). In addi-

tion, the geographical data were obtained from the Research Data Archive of National Center for Atmospheric Research (NCAR) (http://www2.mmm.ucar.edu/wrf/users/downloads.html). The emission inventories used in this study included the 2000-based Regional Emission Inventory in ASia (REAS) (Kurokawa et al., 2013) and the 2010-based Multi-resolution Emission Inventory for China (MEIC) (He, 2012), both of which were processed by the Sparse Matrix Operating Kernel Emission (SMOKE) model. The biogenic emissions were calculated by the Model of Emissions of Gases and Aerosols from Nature (MEGAN) (Guenther, 2006). The WRF modeling mainly focused on O_3 episodes with an additional 24 h preceding run as spin-up for each episode, and the integration was conducted separately. In addition, the spatiotemporal patterns of CO and O_3 were simulated by WRF-CMAQ during two O_3 episodes (see Sect. 3.4). The time series of the simulations and observations of CO and O_3 are shown in Fig. S3. Also, Table S3 gives the index of agreements (IOAs) between the simulated and observed meteorological parameters and air pollutants. Within the range of 0–1, higher IOAs represent better agreement between the simulated and observed values (Willmott, 1982). Here, IOA was between 0.51 and 0.84 for the simulation of meteorological parameters. Furthermore, it was not lower than 0.50 for primary air pollutants and reached 0.81 for O_3 simulation at both sites. The model performances were comparable to those reported in previous studies (Cabaraban et al., 2013; Wang et al., 2015). Therefore, we accepted the modeling results in view of the fact that the simulations were only used to qualitatively indicate the interactions between the continental and marine air in this study.

Backward particle release simulations were carried out using HYSPLIT model (Stein et al., 2015) for episode days at WS and TC sites during the entire sampling period (Draxler and Rolph, 2003). The backward particle release simulation, which considers the dispersion processes in the atmosphere, is capable of identifying the history of air masses (Guo et al., 2009; Ding et al., 2013a, b). In this work, we applied the model following a method developed by Ding et al. (2013b).

3 Results and discussion

3.1 Spatiotemporal variations

Table 1 summarizes the meteorological conditions and chemical species observed at WS and TC. Lower temperature (25.7 ± 0.1 °C) and higher relative humidity (82.8 ± 0.4 %) were recorded at the marine site (WS) compared to the suburban site (TC) ($p < 0.01$) (temperature: 26.7 ± 0.1 °C; relative humidity: 67.7 ± 0.5 %). At WS, the solar radiation (635.8 ± 46.9 W m^{-2}) was much higher than that at TC (563.5 ± 46.1 W m^{-2}, $p < 0.01$), while the average wind speed at TC (4.6 ± 0.1 m s^{-1}) was significantly lower than that measured at WS (7.2 ± 0.2 m s^{-1}). The lower wind speed

at TC was related to the roughness of underlying surfaces. However, no statistical differences were found for the average wind direction (about 81°, northeast wind) at the two sites, indicating that the two sites were probably under the influence of similar air masses in most cases.

The NO, NO_2, CO, SO_2 and total VOCs (the sum of NMHCs and carbonyls) had lower average and maximum mixing ratios at WS than those at TC. The lower levels of primary air pollutants at WS were likely the results of fewer local emission sources, faster photochemical consumption (as discussed later) and/or more favorable dispersion conditions (e.g., higher wind speed). In contrast, O_3 was much higher at WS (Table 1), attributable to the enhancements by both meteorological and photochemical effects, as discussed in Sects. 3.2 and 3.3.

Time series of local meteorological parameters and hourly mixing ratios of air pollutants at the two sites are illustrated in Fig. 2a–b. The temporal patterns of wind directions were generally similar at both sites, with the dominance of the southerly winds in August and northeastern winds between September and November. Occasionally, the northwesterly winds from the PRD region were observed.

This sampling campaign witnessed 17 O_3 episodes and 7 near-O_3 episode days at TC, which refers to the days with maximum hourly mixing ratio of O_3 higher than 100 ppbv and within the range of 80–100 ppbv, respectively (80 ppbv was Level I of China National Ambient Air Quality Standard for O_3). At WS, 21 O_3 episodes and 6 near-O_3 episodes were recorded. Specifically, 13 O_3 episode days were simultaneously observed at the two sites, with the rest occurred exclusively at one site. On one hand, the primary air pollutants (CO, SO_2 and NO_x) generally increased during O_3 episodes, implying enhanced O_3 formation potentials from the precursors. On the other hand, O_3 episodes were always accompanied by the synoptic conditions, i.e., tropical cyclone (typhoon in the mature form) and continental anticyclone, and/or mesoscale circulations such as SLB, as detailed in Table S4. For example, the two multi-day O_3 episode events, i.e., 1–8 October and 19–27 October (highlighted in blue in Fig. 2), were strongly associated with continental high pressure. These episode days generally had high temperature, northerly winds and intensive solar radiation, with air flows largely from the inland or the coastal areas. Also, the mixing ratios of CO, NO_2 and SO_2 usually increased during these days, suggesting the accumulation of local air pollutants and/or the increasing contribution from regional transport. In contrast, O_3 episodes under the influence of tropical cyclones (highlighted in orange in Fig. 2) featured high temperature, strong solar radiation and typically calm or moderate northwesterly to northeasterly winds, except for typhoon Haiyan, which occurred on 9–12 November (discussed in Sect. 3.2.1). These conditions were all conducive to the formation and accumulation of O_3. Additionally, SLB was also an important factor regulating O_3 pollution in this region

Table 1. Descriptive statistics of meteorological parameters and trace gases at the two sites during the sampling period.

Parameter	WS		TC	
	Mean ± 95 % C.I.	Max.	Mean ± 95 % C.I.	Max.
Temperature (°C)	25.7 ± 0.1	32.8	26.7 ± 0.1	35.4
Relative humidity (%)	82.8 ± 0.4	98.9	67.7 ± 0.5	96.8
Solar radiation (W m^{-2})[a]	635.8 ± 46.9	1026.8	563.5 ± 46.1	910.0
Wind speed (m s^{-1})	7.2 ± 0.2	23.8	4.6 ± 0.1	13.8
Wind direction (°)	81.3	–	80.9	–
O_3 (ppbv)	51.3 ± 1.2	173.0	30.0 ± 1.0	159.9
NO (ppbv)	0.7 ± 0.1	21.0	14.0 ± 0.8	115.7
NO_2 (ppbv)	4.3 ± 0.3	49.3	25.0 ± 0.6	104.2
CO (ppbv)	251.4 ± 6.5	727.7	560.5 ± 6.3	1047.9
SO_2 (ppbv)	2.4 ± 0.1	12.2	5.9 ± 0.1	19.1
NMHCs (ppbv)	12.7 ± 1.1	32.9	17.7 ± 1.7	60.0
Carbonyls (ppbv)	7.9 ± 0.7	16.3	9.2 ± 0.7	26.5

[a] Average of the daily maximum solar radiation. C.I. denotes confidence interval.

during O_3 episodes (Table S4). Detailed discussions can be found in Sect. 3.2.3.

3.2 Meteorological influence on O_3 mixing ratios

Descriptive statistics of meteorological parameters during O_3 episode and non-episode days are summarized in Table 2. On episode days the wind speed and relative humidity were lower whereas solar radiation was stronger at both sites, suggesting that this type of weather condition was conducive to the formation and accumulation of tropospheric O_3. Furthermore, the wind direction during non-episode days was predominantly from the east (SCS), while during episode days the winds mainly came from the north and northeast, which might bring more pollutants from the urban areas of Hong Kong and inland PRD to the sampling sites. The characteristics of O_3 pollution under different weather conditions are discussed below.

3.2.1 Tropical cyclones

Tropical cyclone (low-pressure system) is one of the main meteorological conditions conducive to the occurrence of O_3 episodes in Hong Kong (Yin, 2004; Ling et al., 2013). In this study, 7 episode days and 3 near-episode days were closely associated with five tropical cyclones (i.e., Trami, Usagi, Wutip, Nari and Krosa) (Table S4 and Fig. S4). For example, Trami caused the worst O_3 episode on 21 August with the highest peak hourly O_3 mixing ratios of 160 and 173 ppbv at TC and WS, respectively. These episode or near-episode days usually appeared 1–2 days before the arrival of the tropical cyclones, because the large-scale peripheral subsidence of the tropical cyclones usually creates the meteorological conditions favorable to the formation and accumulation of O_3, such as inversion layer, high temperature, low humidity, intensive light and weak winds (Wang et al.,

1998; Yin, 2004). The tropical cyclones also cause anticlockwise air flows at their outskirts, affecting the wind directions and subsequent the regional transport of air pollution. Figure 3 illustrates surface wind fields and air movement 2 days (i.e., 20–21 September) before the occurrence of Usagi as an example. It can be seen that when Usagi approached southeastern area of Hong Kong, it led to weak northeasterly and later northwesterly winds which potentially delivered O_3 and its precursors from highly polluted inland PRD region to the sampling sites (Yin, 2004; Wei et al., 2016; Wang et al., 2017). The wind speed was lower than 4 m s^{-1} at the sampling sites and in their surrounding area on 20 September (Fig. 3a), and it gradually increased the next day (21 September) with the approach of the tropical cyclone (Fig. 3b). It is noteworthy that the rarely occurring westerly and northwesterly winds caused tropical cyclones that resulted in unsynchronized occurrence of O_3 episodes between the two sites (Fig. 3c, d). Namely, high O_3 values were observed at TC only on 20 September, while O_3 started to increase at WS on the next day (21 September). This discrepancy might indicate the transport of O_3 and/or its precursors from terrestrial area to the offshore site driven by tropical cyclone.

Please note that not all tropical cyclones would cause high levels of O_3. For example, the tropical cyclone Haiyan observed on 9–12 November over the SCS did not cause high O_3 levels (Fig. 2b). Because the origin of Haiyan was at a lower latitude (southern Guam) and it moved on the waters southwest of PRD (Fig. S4), the anticlockwise air flow caused easterly and southeasterly winds in the north and northeast outer band of Haiyan. The winds originated from the SCS brought in clean marine air to the sampling sites, resulting in dilution and dispersion of local air pollutants.
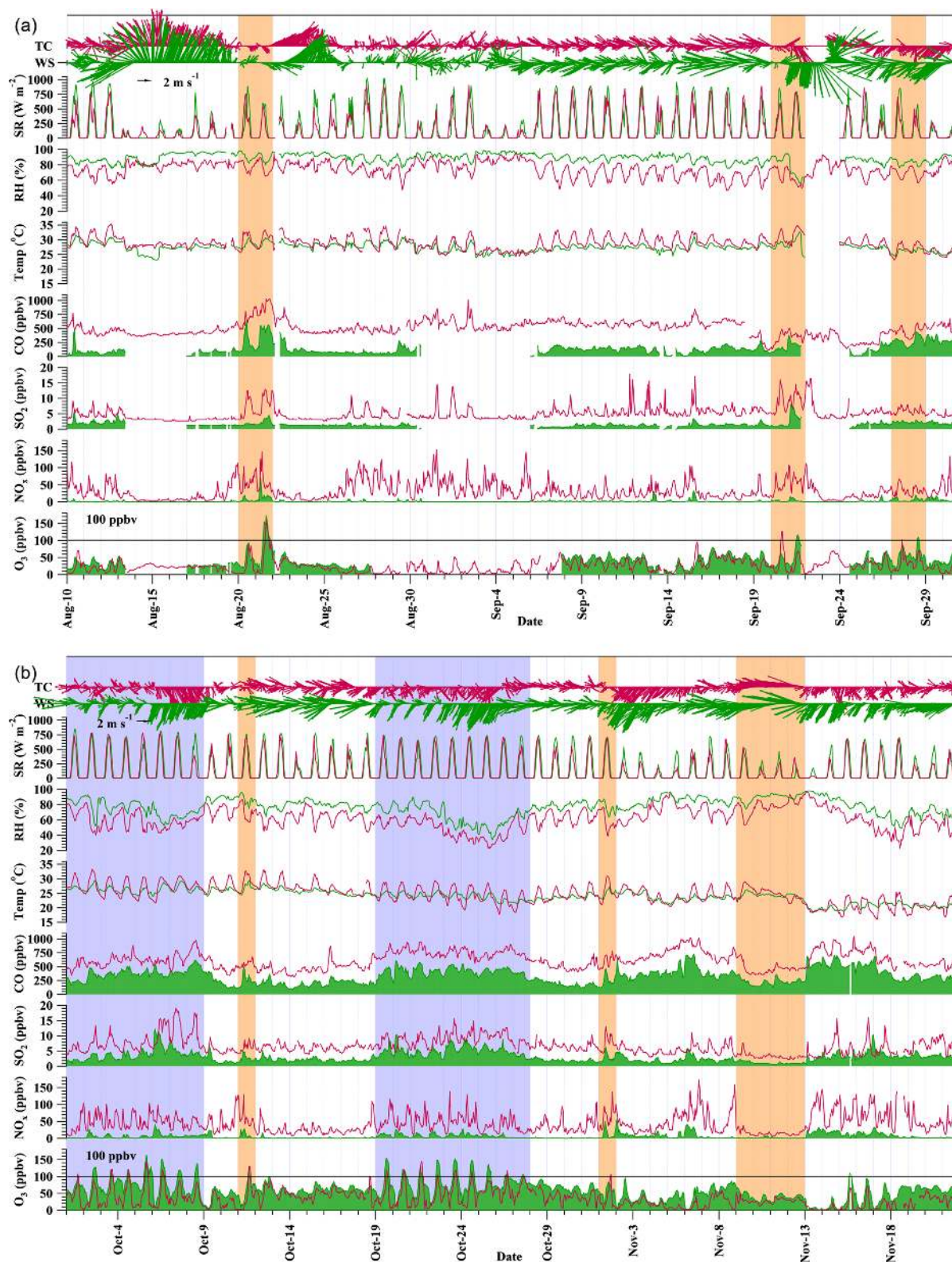
Figure 2. Time series of trace gases and meteorological parameters observed for the sampling period of 10 August–30 September **(a)** and 1 October–21 November **(b)** at WS (green) and TC (red). The black line of 100 ppbv is the threshold for O$_3$ episode definition. The dates seriously affected by continental high pressure and tropical cyclones are shaded in blue and orange, respectively. Note that there are some data missing in these months due to extremely bad weather conditions and instrumental failure.

Table 2. Descriptive statistics (mean $\pm$ 95 % C.I.) of meteorological parameters at the two sites during O_3 episodes and non-O_3 episodes days.

Parameter	WS		TC	
	O_3 episode	Non-O_3 episode	O_3 episode	Non-O_3 episode
Temperature ($^\circ$C)	25.3 ± 0.2	25.8 ± 0.1	26.3 ± 0.3	26.8 ± 0.2
Wind speed ($\mathrm{m\,s^{-1}}$)	5.3 ± 0.2	7.7 ± 0.2	3.7 ± 0.2	4.8 ± 0.1
Wind direction ($^\circ$)	45.1	89.1	19.5	86.8
Relative humidity (%)	71.7 ± 1.2	85.7 ± 0.4	58.4 ± 1.4	69.6 ± 0.6
Solar radiation ($\mathrm{W\,m^{-2}}$)[a]	723.2 ± 26.1	613.7 ± 57.6	699.0 ± 29.1	537.0 ± 53.1

[a] Average of the daily maximum solar radiation. C.I. denotes confidence interval.
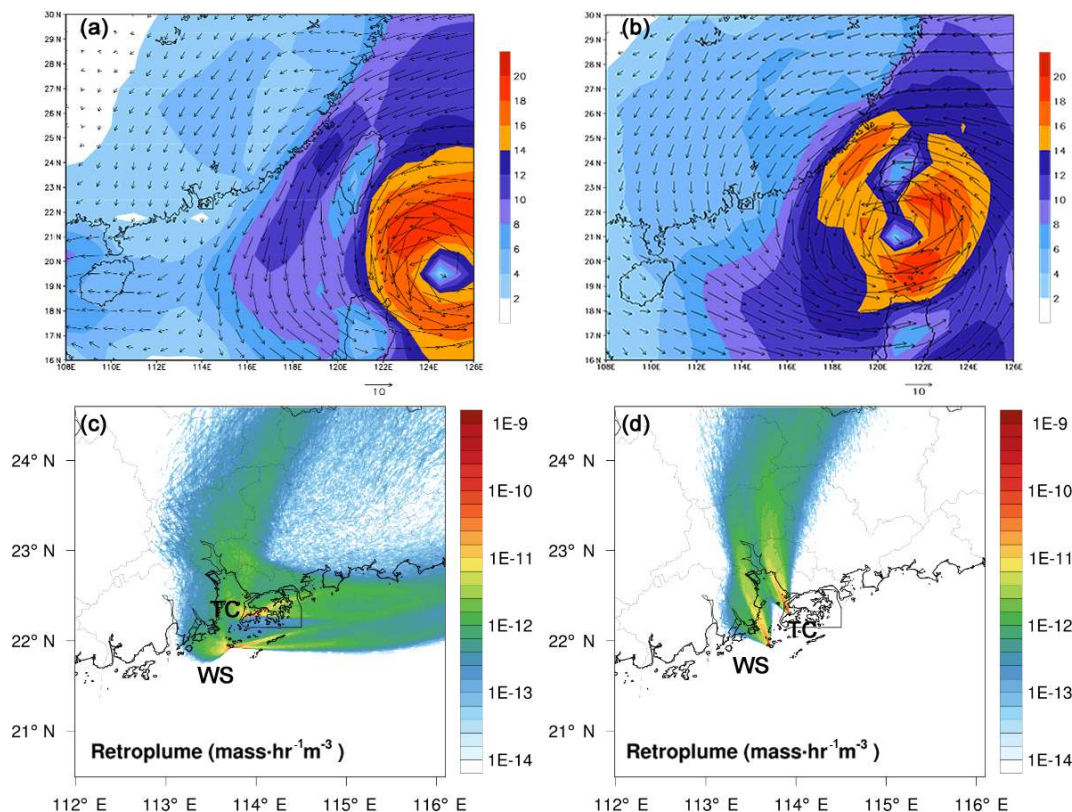
Figure 3. Model-simulated 10 m wind vectors (arrows) and wind speed (shaded, unit: $\mathrm{m\,s^{-1}}$), as well as the distribution of air mass concentrations (unit: $\mathrm{mass\,h^{-1}\,m^{-3}}$) at the 100 m height level simulated by HYSPLIT Lagrangian backward particle release model with WS and TC as the starting points 2 days (20 September 2013) before **(a, c)** and 1 day (21 September 2013) before **(b, d)** the arrival of Usagi.

3.2.2 Continental anticyclones

In addition to tropical cyclones, the continental anticyclone (high-pressure system) was frequently observed in the region, which often caused high O_3 concentrations. For example, two multi-day O_3 episodes (1–8 and 19–27 October) occurred at the sampling sites when there were intensive continental anticyclones and weak Western Pacific Subtropical High (WPSH) to the north of Hong Kong (see Fig. S5 as examples). The SLBs also occurred occasionally during the first several days of the two continental high-pressure sys-

tems when the synoptic winds were relatively weak (i.e., 2–5 and 19–21 October). Under the continental anticyclones, the northeasterly and easterly winds brought in densely polluted air from the inland (Fig. 2b) to the coastal areas of the SCS. For example, the CO mixing ratios were significantly elevated during these episode days, with an average of 409 and 683 ppbv at WS and TC, respectively, which were higher than other episode days. The continuous input of exotic air pollutants provided essential "fuel" to local photochemical production of O_3, leading to the severe multi-day O_3 episodes.
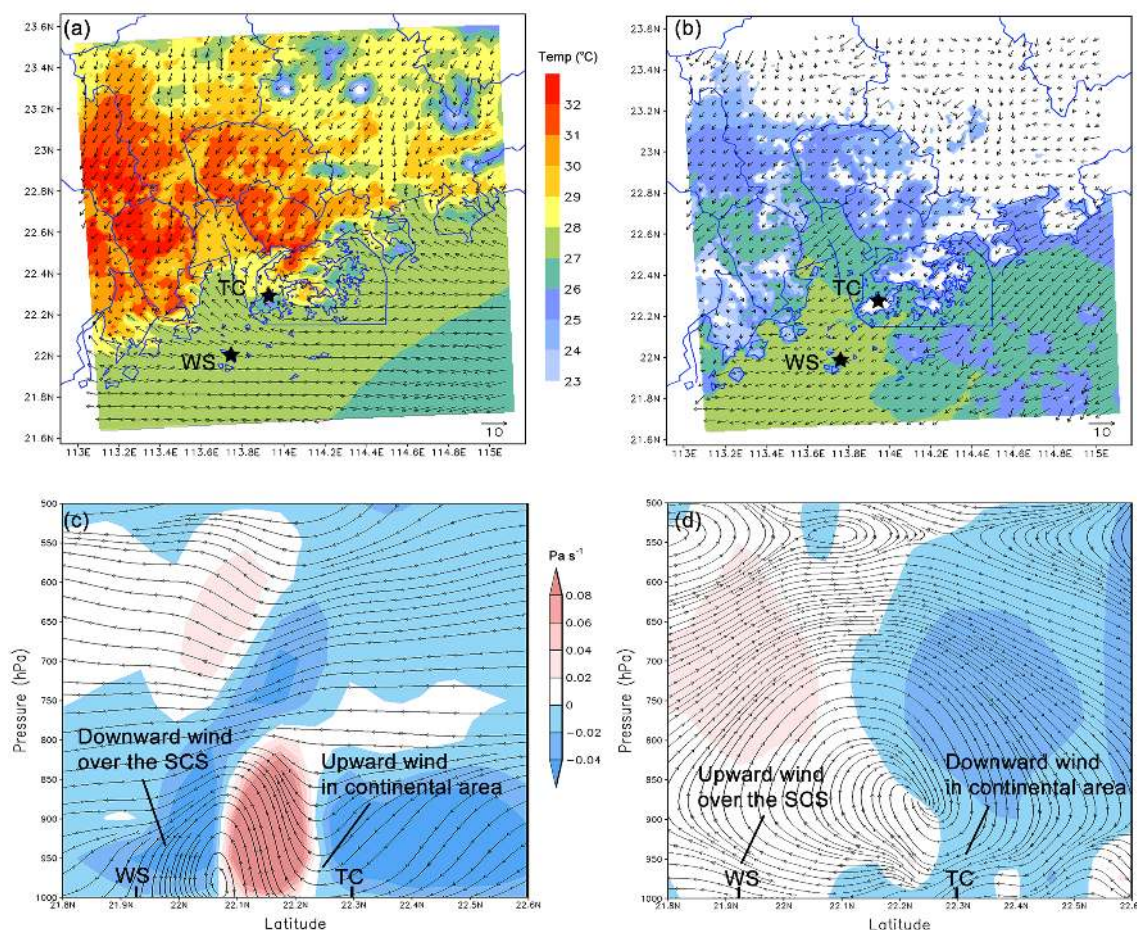
Figure 4. SLB circulation on 3–4 October 2013, showing surface wind pattern (arrows) and temperature (color) at 17:00 on 3 October **(a)** and at 04:00 on 4 October **(b)**. Vertical cross section (taken over a longitude of 113.85° E, mean of the longitudes of TC and WS) depicting the $v-w$ wind stream (arrow) and the index of $\omega \cdot 100$ (color) at 17:00 on 3 October **(c)** and at 04:00 on 4 October **(d)**. For panels **(c)** and **(d)**, the blue color (negative) and light red color (positive) present downward and upward winds, respectively. Panels **(a)** and **(c)** represent a sea breeze, and panels **(b)** and **(d)** show a land breeze. Note that ω is the vertical velocity in isobaric coordinates.

3.2.3 Sea–land breeze circulation

During the sampling period, SLB circulations in the study area were identified on 21 out of 104 sampling days. The occurrence frequency was comparable to that reported by Zhang and Zhang (1997), who discovered 70 SLB days in a year in the same region. In this study, 12 O_3 episode days were thought to be influenced by SLB (see Table S4), with 5 of them (27–28 September, 11–12 October and 1 November) under the dominance of tropical cyclones (i.e., Wutip, Nari and Krosa) and the other 7 days in association with the continental anticyclones. In addition to the effects of tropical cyclones and continental anticyclones discussed above, SLB also posed a non-negligible impact on O_3 pollution in these cases.

SLB circulation is driven by sea–land thermal difference and topographic conditions and usually happens when the synoptic winds are weak (Liu et al., 2002; Lo et al., 2006;

Lu et al., 2009). On a typical SLB day, wind blows onshore during the day (sea breeze) and offshore in the evening (land breeze). However, the transition time of breezes in this study was found to vary in a wide range. The sea breeze switched to land breeze between 00:00 and 08:00 with a median of 03:00 for breeze shifting, and 11:00–18:00 with a median of 14:00 was the time when land breeze turned to sea breeze. Ding et al. (2004) also reported this phenomenon and pointed out that the start time of sea breezes in Hong Kong was generally delayed to noontime due to the synoptic northerly winds blowing from the continental areas to the SCS, particularly on O_3 episode days when northerly winds dominated in Hong Kong. For example, the sea breeze commenced at 15:00 on 3 October and transited to land breeze at 04:00 on 4 October (Fig. 4). Figure 4a and b depict the surface wind fields with a sea breeze and a land breeze, respectively. The vertical wind fields with the sea breeze and land breeze are presented in Fig. 4c and d, respectively. Surface and vertical SLB cir-

culations were clearly seen in these panels of Fig. 4. The mesoscale circulations caused by SLB might promote the interactions between the continental (TC) and marine (WS) atmospheres. Specifically, the primary air pollutants observed at TC could be transported to WS by land breeze. Moreover, the air masses could return to TC after sufficient photochemical evolutions over the SCS, during which O_3 might also be elevated in the continental areas.

3.3 Chemical characteristics of air masses

3.3.1 Chemical composition

To inspect the chemical characteristics of air masses on O_3 episode days and non-O_3 episode days, chemical species are statistically summarized at the two sites (Table 3). As expected, the levels of all pollutants (i.e., O_3, NO_2, CO, SO_2, NMHCs and carbonyls) were significantly higher on O_3 episode days for both sites ($p < 0.05$), except for the comparable or even lower NO due to its titration to O_3 (see Sect. 3.3.2). Table S5 shows statistics of the top 10 NMHC and the top 3 carbonyl species observed during O_3 episodes and non-episodes at the two sites. The dominant species were quite similar regardless of episode or non-episode days at both sites. The higher concentrations of both primary and secondary pollutants on episode days than those on non-episode days were likely due to more intense photochemical reactions, more local pollutant accumulation as well as the regional transport of more highly polluted air masses. In contrast, the similar NMHCs composition at both sites during both episodes and non-episodes indicated somewhat interaction of air masses between the two sites regardless of O_3 levels.

It is worth mentioning that O_3 was much higher at WS than that at TC during both episodes and non-episodes ($p < 0.01$), with an average difference of 30.2 and 16.7 ppbv, respectively (Table 3), though the levels of O_3 precursors (i.e., NO_x and VOCs) at WS were lower. Insight into VOC ratios found that ethene / ethane (0.5 ± 0.04) and toluene / benzene (2.2 ± 0.5) at WS were significantly ($p < 0.05$) lower than those at TC (0.7 ± 0.1 and 2.9 ± 0.4, respectively), likely indicating that the air masses at WS were more aged (Guo et al., 2007). Therefore, the higher O_3 at WS might be partially attributable to the aging of air masses (e.g., during the transport of continental air).

3.3.2 Influence of NO titration

Apart from the age of air masses, NO titration is another important factor influencing O_3 concentration. In areas with high NO levels, the NO titration ($O_3 + NO \rightarrow NO_2 + O_2$) is a main process consuming O_3. In this study, the average NO mixing ratio at TC was 14.0 ± 0.8 ppbv, compared to 0.7 ± 0.1 ppbv at WS (Table 1). The much lower NO at WS implied weaker titration to O_3, which enabled the sur-

vival of more O_3 and caused substantial residual O_3 at WS, particularly at nighttime when there were no photochemical reactions (Figs. 2 and S6). Another direct evidence of NO titration effect was the trough of O_3 during the morning rush hours (06:00–07:00), together with an increase of NO_2 (Fig. S6). Furthermore, the total oxidants ($O_x = O_3 + NO_2$), which are usually adopted to take into account the NO titration influence, were comparable ($p > 0.05$) between TC and WS with mean values of 83.3 ± 3.7 and 81.6 ± 2.9 ppbv during O_3 episodes and 49.4 ± 1.0 and 47.8 ± 1.0 ppbv during non-episodes, respectively (Table 3). This was reasonable in view of the interactions between the two sites. However, the remarkably higher O_3 and lower NO at WS indicated that NO titration was a determinant factor regulating the O_3 levels at both sites.

Moreover, NO titration is generally more significant on high-O_3 days, resulting in higher NO_2 / NO ratios due to the conversion of NO to NO_2 by O_3. Indeed, the mean NO_2 / NO ratios increased from 4.7 ± 0.5 at WS and 1.5 ± 0.2 at TC during non-episodes to 12.7 ± 1.1 and 3.4 ± 0.4 during O_3 episodes, respectively, implying that more O_3 was titrated by NO during episodes. As a result, NO at TC was lower ($p < 0.01$) during O_3 episodes than during non-episodes (Table 3). It is noteworthy that NO at WS was on the same level between O_3 episode and non-O_3 episode days ($p > 0.05$). This probably related to the weak titration at this marine site due to the trivial NO concentrations in both periods, as well as the counteracting effect of the increased transport of NO under northerly winds against the enhanced titration during O_3 episodes.

The aforementioned discussion demonstrated that NO titration played an important role in altering O_3 distribution, especially on O_3 episodes days. The lower NO (weaker NO titration) partially resulted in the higher O_3 concentrations observed at WS.

3.3.3 Atmospheric oxidative capacity and O_3 production rate

O_3 formation is driven by the transformation and recycling of oxidative radicals, including OH, HO_2 and RO_2, collectively referred to as RO_x hereafter. The production and loss rates of these radicals, and their equilibrium concentrations on the canister sampling days were simulated by the PBM-MCM model, as shown in Fig. S7. We noticed that WS featured significantly higher levels of these oxidative radicals on average ($p < 0.05$). The daytime (07:00–19:00 LT) average OH concentration at TC and WS was $(1.5 \pm 0.4) \times 10^6$ molecules cm^{-3} and $(5.5 \pm 0.9) \times 10^6$ molecules cm^{-3} during O_3 episodes, respectively. Consistently, HO_2 and RO_2 at WS were well above those at TC (Table 3). This pattern was also applicable between the two sites during non-episodes. Furthermore, while the difference in OH concentration became less on non-episode days, the gaps for peroxy radicals (HO_2 and

Table 3. Descriptive statistics (mean $\pm$ 95 % C.I.) of measured air pollutants and simulated OH, HO$_2$ and RO$_2$ at the two sites during O$_3$ episodes and non-O$_3$ episodes days.

Parameter	WS		TC	
	O$_3$ episode	Non-O$_3$ episode	O$_3$ episode	Non-O$_3$ episode
O$_3$ (ppbv)	74.3 ± 3.0	43.9 ± 1.0	44.1 ± 3.6	27.2 ± 0.8
O$_x$ (ppbv)	81.6 ± 2.9	47.8 ± 1.0	83.3 ± 3.7	49.4 ± 1.0
NO (ppbv)	0.9 ± 0.2	0.5 ± 0.2	11.5 ± 1.4	14.5 ± 0.9
NO$_2$ (ppbv)	8.5 ± 0.9	2.0 ± 0.5	39.2 ± 1.7	22.2 ± 0.6
CO (ppbv)	391.4 ± 9.1	209.4 ± 6.8	652.9 ± 16.0	541.9 ± 6.5
SO$_2$ (ppbv)	4.3 ± 0.2	1.9 ± 0.1	8.1 ± 0.3	5.5 ± 0.1
NMHCs (ppbv)	17.7 ± 1.4	9.6 ± 1.2	20.2 ± 2.2	16.8 ± 2.1
Carbonyls (ppbv)	10.3 ± 0.8	5.4 ± 0.4	12.0 ± 1.3	8.1 ± 0.7
NO$_2$ / NO (ppbv / ppbv)	12.7 ± 1.1	4.7 ± 0.5	3.4 ± 0.4	1.5 ± 0.2
Simulated OH ($\times 10^6$ molecules cm^{-3})	5.5 ± 0.9	4.4 ± 0.6	1.5 ± 0.4	2.1 ± 0.3
Simulated HO$_2$ ($\times 10^7$ molecules cm^{-3})	29 ± 4.9	45 ± 4.2	2.0 ± 1.0	2.6 ± 0.7
Simulated RO$_2$ ($\times 10^7$ molecules cm^{-3})	19 ± 3.8	47 ± 6.2	1.2 ± 0.6	1.4 ± 0.4

[a] Average of the daily maximum solar radiation. C.I. denotes confidence interval. O$_x$ = O$_3$ + NO$_2$.

RO$_2$) between TC and WS widened, as listed in Table 3. From non-episodes to episodes, OH increased at WS alongside with the deceases of HO$_2$ and RO$_2$, likely indicating more conversion of HO$_2$ to OH by NO, which is an important pathway leading to O$_3$ formation. Details about this were shown later.

To explain the inter-site differences of the concentrations of oxidative radicals and the variations between O$_3$ episodes and non-episodes, Fig. S7 also provides the breakdowns of the production and loss rates of OH, HO$_2$ and RO$_2$ at TC and WS, separately. Overall, the reaction between HO$_2$ and NO dominated the production of OH at both sites, with the contribution of 69.4 ± 2.0 % and 81.0 ± 1.5 % at TC and WS, respectively. While the photolysis of HONO ranked second in the production of OH at TC (22.2 ± 2.1 %), the contribution of this pathway to OH production at WS (3.7 ± 0.6 %) was overstepped by O$_3$ photolysis (13.1 ± 1.6 %). This discrepancy was associated with the higher HONO and lower O$_3$ at TC (Fig. S1 and Table 3). As expected, the production rate of OH through HO$_2$ reacting with NO experienced the most significant increase from $1.4 \pm 0.2 \times 10^7$ molecules cm^{-3} s^{-1} during non-episodes to $3.6 \pm 0.6 \times 10^7$ molecules cm^{-3} s^{-1} during O$_3$ episodes at WS, which explained more than 90 % of the increase of the total OH production. In terms of the losses of OH, reaction between OH and NO$_2$ was the largest sink of OH at TC. However, OH-initiated oxidations of VOCs consumed most (52.7 ± 1.8 %) of OH at WS. This was reasonable in view of the much more abundant NO$_2$ at TC than at WS, in contrast to the smaller difference in NMHCs between the two sites (Table 3). Since OH can generally be recycled from the oxidation of VOCs, the lower OH at TC was likely caused by the lower O$_3$ photolysis and higher consumption of OH by NO$_2$, despite the more intensive HONO photolysis. The overall oxidation rate of

VOCs by OH was employed to indicate the atmospheric oxidative capacity in previous studies (Elshorbany et al., 2009; Xue et al., 2016). In this study, we found that the oxidation rate of VOCs at TC ($6.1 \pm 2.1 \times 10^6$ molecules cm^{-3} s^{-1} during O$_3$ episodes and $5.7 \pm 0.9 \times 10^6$ molecules cm^{-3} s^{-1} during non-episodes) was remarkably ($p < 0.05$) lower than that at WS (O$_3$ episode: $15 \pm 2.5 \times 10^6$ molecules cm^{-3} s^{-1} and non-episode: $8.9 \pm 1.3 \times 10^6$ molecules cm^{-3} s^{-1}). The results revealed that the atmospheric oxidative capacity at TC was weaker than at WS for both O$_3$ episodes and non-episodes, inconsistent with the findings of Elshorbany et al. (2009) and Xue et al. (2016), who concluded that the atmospheric oxidative capacity was higher in more polluted environments due to the fact that the atmospheric oxidative capacity is positively proportional to the VOCs and OH levels. Both Elshorbany et al. (2009) and Xue et al. (2016) reported very high mixing ratios of VOCs (e.g., toluene of 9.5 and 6.3 ppbv, respectively) in the polluted cases, which explained the strong atmospheric oxidative capacity. However, in this study, it is more likely that the higher NO$_x$ at TC consumed more OH and resulted in lower oxidative capacity than at WS, despite the slightly higher VOCs at TC (Table 3).

For HO$_2$, RO$_2$ reacting with NO accounted for 56.7 ± 1.1 % and 60.7 ± 1.0 % of HO$_2$ production at TC and WS, respectively. Oxidation of CO by OH was also an important pathway leading to HO$_2$ formation, second to RO$_2$ + NO at both sites. At TC, HO$_2$ was almost exclusively depleted by NO. However, 10.8 ± 1.8 % and 6.5 ± 0.8 % of the HO$_2$ losses were attributable to HO$_2$–RO$_2$ and HO$_2$–HO$_2$ reactions at WS, though HO$_2$ + NO was responsible for the most fraction (82.7 ± 2.6 %) of HO$_2$ losses. We believe that the more significant self-consumption of peroxy radicals at WS was closely related to the low NO$_x$ there, which hampered the transfer of oxygen atom from peroxy
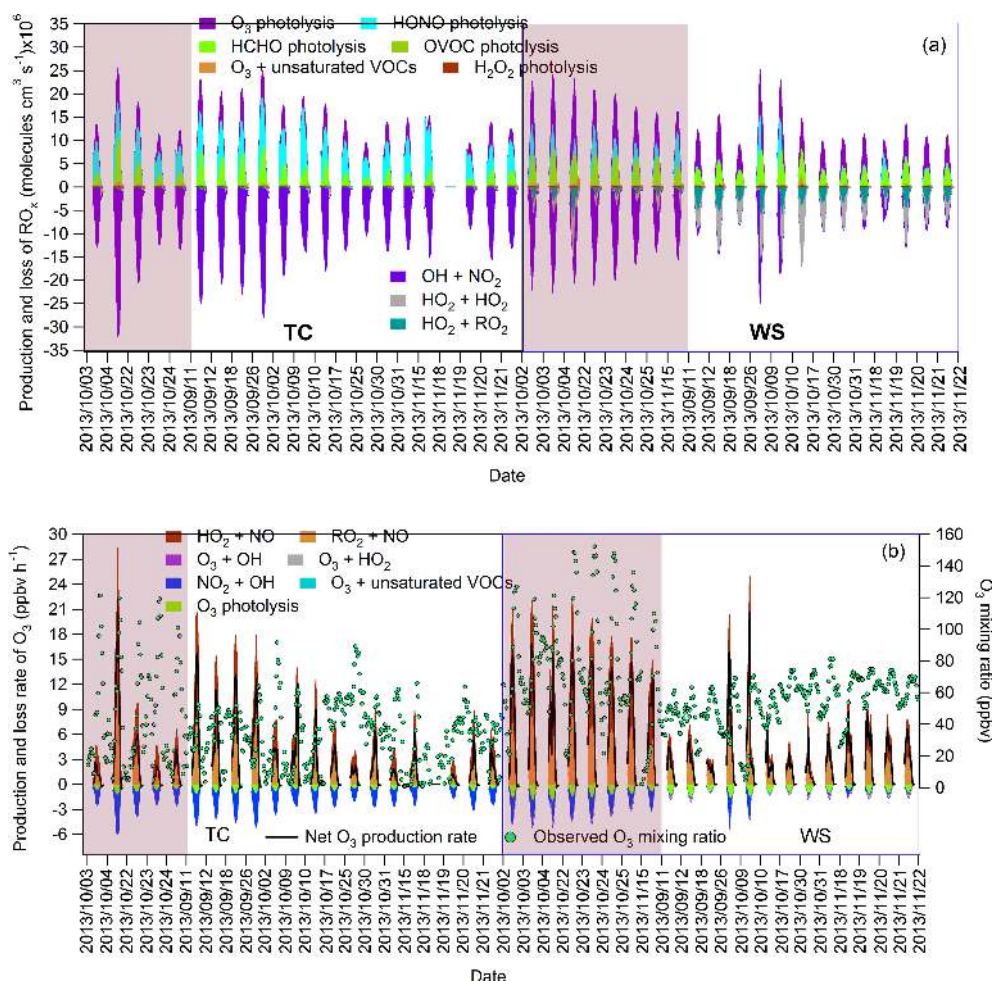
Figure 5. Daytime (07:00–19:00 LT) variations of the simulated production and loss rates of **(a)** RO_x and **(b)** O_3 at TC (left panel) and WS (right panel). O_3 episode days are highlighted in red background. The dates are not consecutive due to the discontinuous canister sampling of VOCs.

radicals to NO and further formation of O_3. This was confirmed by the enhanced losses of HO_2 through reactions with HO_2 itself and RO_2 from 3.0 ± 1.2 % during O_3 episodes to 24.9 ± 3.4 % during non-episodes at WS, because NO_x was more scarce during non-episodes at this site (Table 3). Similarly, in contrast to the negligible influence of RO_2 reacting with HO_2 on RO_2 budget at TC, HO_2–RO_2 reactions played important role in losses of RO_2 at WS, particularly on non-episode days (Fig. S7). When OH, HO_2 and RO_2 were summed up, the production and loss rate of RO_x were obtained, as shown in Fig. 5a. Under such circumstance, the transformation and recycling pathways among these radicals can be neglected. For example, OH-initiated oxidation of VOCs consumes OH, which, however, generates RO_2. Therefore, these reactions were not considered as sources or sinks of RO_x. On one hand, HONO photolysis was the largest source of RO_x at TC (53.7 ± 2.6 %), followed by the photolysis of HCHO (21.1 ± 1.6 %) and O_3 (18.7 ± 1.5 %). However, O_3 photolysis ranked the first among the sources

of RO_x at WS with the contribution of 38.6 ± 2.3 %, higher than the contributions from HCHO photolysis (34.3 ± 1.4 %) and HONO photolysis (18 ± 2.5 %). On the other hand, while the reaction between OH and NO_2 served as the sole sink of RO_x at TC, it only explained 50 % of RO_x sink at WS with the other half attributable to self-consumption of peroxy radicals.

Furthermore, the production and loss rates of O_3 were simulated (Fig. 5b). Despite the increased O_3 mixing ratio during episodes (Table 3), there was no significant change in net O_3 production between O_3 episodes (2.5 ± 1.0 ppbv h^{-1}) and non-episodes (2.5 ± 0.5 ppbv h^{-1}) at TC ($p > 0.05$), suggesting that regional transport might play critical roles in regulating O_3 levels at TC. In fact, previous studies (Huang et al., 2006; Jiang et al., 2008) have repeatedly confirmed that O_3 pollution at this site could be aggravated under northerly winds and/or downdraft on the periphery of typhoon. In contrast, the net O_3 production increased remarkably from non-episodes (2.8 ± 0.5 ppbv h^{-1}) to O_3 episodes
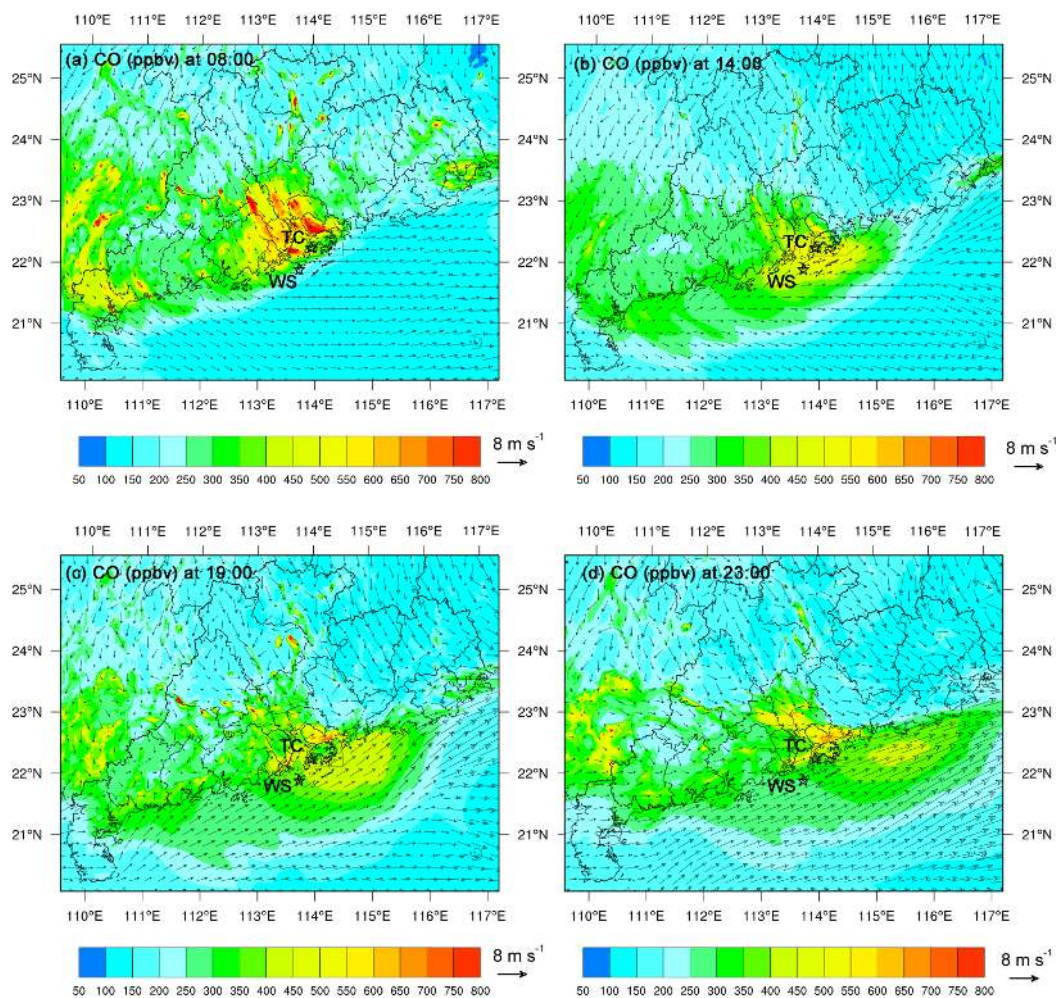
Figure 6. Spatial distribution of CO at 08:00 **(a)**, 14:00 **(b)**, 19:00 **(c)** and 23:00 **(d)** on 21 August simulated by WRF-CMAQ, taken as an example of the "outflow" interaction pattern. Arrows in the figure represent the surface wind field.

$(6.6 \pm 1.1 \, \text{ppbv} \, \text{h}^{-1})$ at WS. Obviously, O_3 production at WS was much higher than at TC during O_3 episodes, while they were comparable during non-episodes. This was likely due to the more abundant peroxy radicals (RO_2 and HO_2) at WS than at TC, in addition to the increased NO_x during O_3 episodes which enhanced the reactions between the peroxy radicals and NO (increasing O_3 formation). Insight into the O_3 production pathways found that the reaction rates of $RO_2 + NO$ and $HO_2 + NO$ were significantly enhanced from 1.6 ± 0.2 and $2.0 \pm 0.4 \, \text{ppbv} \, \text{h}^{-1}$ during non-episodes to 3.2 ± 0.5 and $5.2 \pm 0.9 \, \text{ppbv} \, \text{h}^{-1}$ during O_3 episodes, respectively. Our recent study (Wang et al., 2018) revealed that O_3 formation at WS was in a transition regime and much more sensitive to NO_x during non-episodes, when O_3 production through peroxy radicals reacting with NO was seriously limited by the low NO_x. During O_3 episodes, with the increase O_3 precursors (particularly NO_x), these reactions were accelerated and the net O_3 production increased

substantially. Detailed discussion on the O_3 photochemistry at WS can be found in our recent publication (Wang et al., 2018).

3.4 Impact of air mass interaction on O_3 pollution in coastal areas

Driven by various weather systems (e.g., continental anticyclones, WPSH, tropical cyclones and SLBs), continental and marine air masses frequently interact with each other in the coastal areas. When continental air masses intrude into marine atmosphere, the chemical composition and atmospheric oxidative capacity over the marine atmosphere will be altered by the introduction of anthropogenic pollutants. Taking 21 August as an example, when the sampling sites (TC and WS) were under northwesterly to southwesterly winds caused by tropical cyclone (Fig. 2a), the maximum hourly O_3 reached 160 and 173 ppbv at TC and WS, respectively.
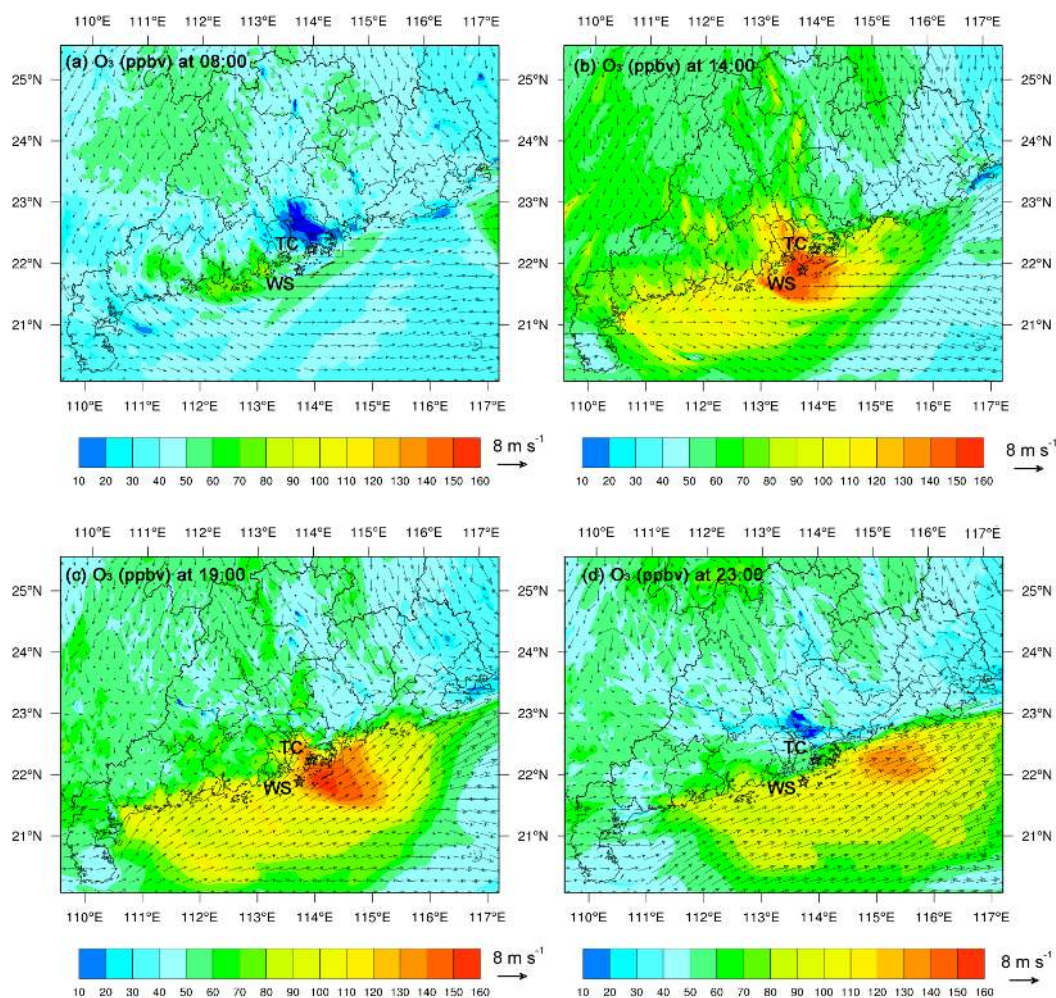
Figure 7. Spatial distribution of O_3 at 08:00 **(a)**, 14:00 **(b)**, 19:00 **(c)** and 23:00 **(d)** on 21 August simulated by WRF-CMAQ, taken as an example of the "outflow" interaction pattern. Arrows in the figure represent the surface wind field.

Correspondingly, the primary air pollutants all stayed on high levels compared to those during non-episodes (Fig. 2a). Since WS was almost free of anthropogenic emissions, the great abundances of both primary and secondary air pollutants implied the influence of continental pollution on air quality at this site. Figures 6–7 depict the spatial distributions of CO and O_3 over the region of interest at selective times (08:00, 14:00, 19:00 and 23:00) on 21 August, respectively. CO is presented as an example of primary air pollutants emitted from anthropogenic sources. The spatiotemporal patterns of CO and O_3 were simulated by WRF-CMAQ. Noticeably, the model reproduced well the high level of CO in PRD region at 08:00, which was reasonable in view of the vehicular emissions in urban areas during morning rush hours. However, under the dominance of northwesterly winds in the morning, the center of high CO moved to the coastal areas. Even though the winds changed to southwesterly at noon, CO concentration over the SCS was still remarkably elevated ac-

cording to the simulated results at 14:00. Further, the spatial distribution of CO at 19:00 and 23:00 confirmed the continuous movement of the polluted air masses away from the land under southwesterly winds. It should be noted that the increase of CO in PRD region at 19:00 and 23:00 was most likely caused by the vehicle emissions during evening rush hours. Overall, the dynamic distribution of CO in the study area clearly indicated the interaction between continental and marine atmospheres. As a result of the intrusion of continental air, a high level of O_3 was simulated over the SCS at 14:00 (Fig. 7b), which was comparable to the observed value (148 ppbv) at WS. Moreover, O_3 was even higher over the SCS than that in continental area, mainly due to the more aged air masses, lower NO titration and higher oxidative capacity of the atmosphere (see Sect. 3.3). Consistent with CO, the center of high O_3 moved away from the land. At 19:00, the O_3-laden air mass penetrated the SCS ∼ 300 km, causing ∼ 8000 km^2 water area (8 times the area of Hong Kong) un-
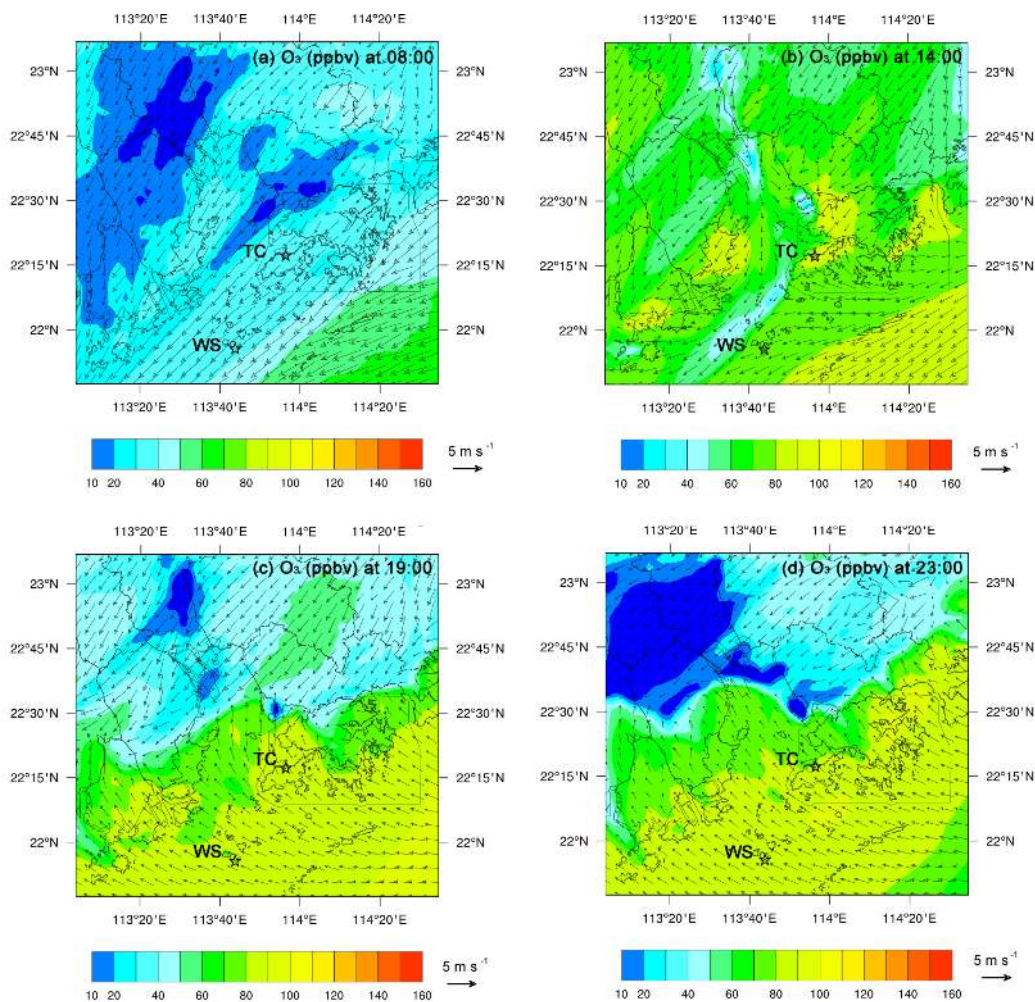
Figure 8. Spatial distribution of O_3 at 08:00 **(a)**, 14:00 **(b)**, 19:00 **(c)** and 23:00 **(d)** on 3 October, taken as an example of the sea–land breeze interaction pattern. Arrows in the figure represent the surface wind field.

der high level of O_3 (> 100 ppbv). This case provided solid evidence of the transport of continental air masses to the SCS, which aggravated air pollution (particularly O_3 pollution) in this offshore area.

In contrast to outflow of continental air masses, the continental area near the coast could also be immersed by oceanic air masses. The arrival of oceanic air masses generally brings substantial marine-originated compounds (e.g., dimethyl sulfide) to the continent and significantly alleviates the anthropogenic air pollution there. In fact, this is one of the main reasons for low-O_3 mixing ratio observed in the PRD region in summertime when southwestern winds prevail (T. Wang et al., 2009; Y. Wang et al., 2017). In this study, it was also found that winds over the ocean increased the concentration of dimethyl sulfide at TC (Fig. S8) and reduced the levels of almost all manmade air pollutants in many cases, mainly in summertime (Fig. 2a).

In contrast, sea breezes carrying elevated O_3 formed over the SCS might build up the terrestrial O_3 in the coastal area in some cases. Figure 8 shows the spatial distribution of O_3 over the study area on 3 October as an example of SLB regulating O_3 formation and distribution (see Fig. 4). Similar to the aforementioned scenario controlled by tropical cyclone, the simulated O_3 at 14:00 was generally higher over the SCS than in the terrestrial area, indicating the transport of polluted air masses from the land to the sea area. This was confirmed by the prevailing northeasterly winds in the morning (08:00 here). However, the O_3-laden air did not move far away from the land subsequently. Instead, it progressively approached the land, leading to increase of O_3 concentration in most parts of Hong Kong. This is because the wind direction in the coastal region changed from northeasterly to southeasterly at 17:00. Namely, the sea breeze appeared in late afternoon, which delivered the high O_3 formed over the SCS to the continental areas near the coast. In fact, the air quality moni-

toring stations deployed in southern Hong Kong by HKEPD also recorded the O_3 peak in the evening when O_3 could not be formed locally (Fig. S9), further confirming the recirculation of O_3-laden air from SCS to coastal areas of Hong Kong under sea breeze. However, the oceanic air did not penetrate further into inland PRD, which was likely stopped by the strong northeasterly winds dominated in the inland areas. Overall, it can be seen that SLB as a common interaction between marine and continental atmospheres played important role in regulating O_3 formation and distribution in coastal region of SCS, which is also applicable to other similar mesoscale environments throughout the world.

4 Conclusions

Coastal regions with dense population, economic prosperity and environmental pollution are common in the world. This study provided an overview of O_3 pollution in warm seasons around a coastal region of the SCS, focusing on the influences of interactions between marine and continental atmospheres on air quality in this subtropical region. The concurrent measurements of primary and secondary air pollutants at TC (a continental site) and WS (a marine site) from August to November 2013 indicated that O_3 was much higher at WS than that at TC, contrary to the more abundant primary air pollutants at TC. At the two sites, O_3 episodes and near-O_3 episodes were frequently observed, which were closely associated with continental anticyclone, tropical cyclone and SLB. In addition to high temperature, strong solar radiation and weak wind, the aforementioned meteorological conditions all favored the transport of polluted air masses from continental areas to the SCS, during which the air pollutants were transformed with the aging of air masses. After arriving in the SCS, the land-originated air pollutants further involved in intensive photochemical reactions with the trait of low NO titration to O_3 and high O_3 production rate, leading to higher O_3 levels in marine atmosphere (WS) than in coastal cities (TC). In addition to the continental outflow that aggravated O_3 pollution over the SCS, SLB as a common interaction in coastal areas also often facilitated the recirculation of O_3 formed over the SCS to the continental areas, building up O_3 concentration in coastal cities under sea breeze. The findings can be extended to other similar regions to advance our understanding of O_3 pollution.

The Supplement related to this article is available online at https://doi.org/10.5194/acp-18-4277-2018-supplement.

References

Adame, J. A., Serrano, E., Bolívar, J. P., and de la Morena, B. A.: On the Tropospheric Ozone Variations in a Coastal Area of Southwestern Europe under a Mesoscale Circulation, J. Appl. Meteorol. Clim., 49, 748–759, https://doi.org/10.1175/2009jamc2097.1, 2010.

Bell, M. L., Goldberg, R., Hogrefe, C., Kinney, P. L., Knowlton, K., Lynn, B., Rosenthal, J., Rosenzweig, C., and Patz, J. A.: Climate change, ambient ozone, and health in 50 US cities, Climatic Change, 82, 61–76, 2007.

Cabaraban, M. T. I., Kroll, C. N., Hirabayashi, S., and Nowak, D. J.: Modeling of air pollutant removal by dry deposition to urban trees using a WRF/CMAQ/i-Tree Eco coupled system, Environ. Pollut., 176, 123–133, 2013.

Chan, C. Y.: Effects of Asian air pollution transport and photochemistry on carbon monoxide variability and ozone production in subtropical coastal south China, J. Geophys. Res., 107, 4746, https://doi.org/10.1029/2002jd002131, 2002.

Cheng, H., Guo, H., Saunders, S., Lam, S., Jiang, F., Wang, X., Simpson, I., Blake, D., Louie, P., and Wang, T.: Assessing photochemical ozone formation in the Pearl River Delta with a photochemical trajectory model, Atmos. Environ., 44, 4199–4208, 2010a.

Cheng, H., Guo, H., Wang, X., Saunders, S. M., Lam, S. H. M., Jiang, F., Wang, T., Ding, A., Lee, S., and Ho, K.: On the relationship between ozone and its precursors in the Pearl River Delta: application of an observation-based model (OBM), Environ. Sci. Pollut. R., 17, 547–560, 2010b.

Cui, J., Deolal, S. P., Sprenger, M., Henne, S., Staehelin, J., Steinbacher, M., and Nedelec, P.: Free tropospheric ozone changes over Europe as observed at Jungfraujoch (1990–2008): An analysis based on backward trajectories, J. Geophys. Res.-Atmos., 116, D10304, https://doi.org/10.1029/2010JD015154, 2011.

Derwent, R. G., Manning, A. J., Simmonds, P. G., Spain, T. G., and O'Doherty, S.: Analysis and interpretation of 25 years of ozone observations at the Mace Head Atmospheric Research Station on the Atlantic Ocean coast of Ireland from 1987 to 2012, Atmos. Environ., 80, 361–368, https://doi.org/10.1016/j.atmosenv.2013.08.003, 2013.

Ding, A. J., Wang, T., Zhao, M., Wang, T. J., and Li, Z. K.: Simulation of sea-land breezes and a discussion of their implications on the transport of air pollution during a multi-day ozone episode in the Pearl River Delta of China, Atmos. Environ., 38, 6737–6750, https://doi.org/10.1016/j.atmosenv.2004.09.017, 2004.

Ding, A. J., Wang, T., Thouret, V., Cammas, J.-P., and Nédélec, P.: Tropospheric ozone climatology over Beijing: analysis of aircraft data from the MOZAIC program, Atmos. Chem. Phys., 8, 1–13, https://doi.org/10.5194/acp-8-1-2008, 2008.

Ding, A. J., Fu, C. B., Yang, X. Q., Sun, J. N., Zheng, L. F., Xie, Y. N., Herrmann, E., Nie, W., Petäjä, T., Kerminen, V.-M., and Kulmala, M.: Ozone and fine particle in the western Yangtze River Delta: an overview of 1 yr data at the SORPES station, Atmos. Chem. Phys., 13, 5813–5830, https://doi.org/10.5194/acp-13-5813-2013, 2013a.

Ding, A. J., Wang, T., and Fu, C. B.: Transport characteristics and origins of carbon monoxide and ozone in Hong Kong, South China, J. Geophys. Res.-Atmos., 118, 9475–9488, 2013b.

Draxler, R. R. and Rolph, G. D.: HYSPLIT (HYbrid Single-Particle Lagrangian Integrated Trajectory) Model, available at: http://www.arl.noaa.gov/ready/hysplit4.html (last access: 26 March 2018), NOAA Air Resources Laboratory, Silver Spring, Maryland, USA, 2003.

Dunlea, E. J., Herndon, S. C., Nelson, D. D., Volkamer, R. M., San Martini, F., Sheehy, P. M., Zahniser, M. S., Shorter, J. H., Wormhoudt, J. C., Lamb, B. K., Allwine, E. J., Gaffney, J. S., Marley, N. A., Grutter, M., Marquez, C., Blanco, S., Cardenas, B., Retama, A., Ramos Villegas, C. R., Kolb, C. E., Molina, L. T., and Molina, M. J.: Evaluation of nitrogen dioxide chemiluminescence monitors in a polluted urban environment, Atmos. Chem. Phys., 7, 2691–2704, https://doi.org/10.5194/acp-7-2691-2007, 2007.

Elshorbany, Y. F., Kurtenbach, R., Wiesen, P., Lissi, E., Rubio, M., Villena, G., Gramsch, E., Rickard, A. R., Pilling, M. J., and Kleffmann, J.: Oxidation capacity of the city air of Santiago, Chile, Atmos. Chem. Phys., 9, 2257–2273, https://doi.org/10.5194/acp-9-2257-2009, 2009.

Fowler, D., Pilegaard, K., Sutton, M. A., Ambus, P., Raivonen, M., Duyzer, J., Simpson, D., Fagerli, H., Fuzzi, S., Schjoerring, J. K., Granier, C., Neftel, A., Isaksen, I. S. A., Laj, P., Maione, M., Monks, P. S., Burkhardt, J., Daemmgen, U., Neirynck, J., Personne, E., Wichink-Kruit, R., Butterbach-Bahl, K., Flechard, C., Tuovinen, J. P., Coyle, M., Gerosa, G., Loubet, B., Altimir, N., Gruenhage, L., Ammann, C., Cieslik, S., Paoletti, E., Mikkelsen, T. N., Ro-Poulsen, H., Cellier, P., Cape, J. N., Horvath, L., Loreto, F., Niinemets, U., Palmer, P. I., Rinne, J., Misztal, P., Nemitz, E., Nilsson, D., Pryor, S., Gallagher, M. W., Vesala, T., Skiba, U., Brueggemann, N.,

Zechmeister-Boltenstern, S., Williams, J., O'Dowd, C., Facchini, M. C., de Leeuw, G., Flossman, A., Chaumerliac, N., and Erisman, J. W.: Atmospheric composition change: Ecosystems-Atmosphere interactions, Atmos. Environ., 43, 5193–5267, https://doi.org/10.1016/j.atmosenv.2009.07.068, 2009.

Guenther, A., Karl, T., Harley, P., Wiedinmyer, C., Palmer, P. I., and Geron, C.: Estimates of global terrestrial isoprene emissions using MEGAN (Model of Emissions of Gases and Aerosols from Nature), Atmos. Chem. Phys., 6, 3181–3210, https://doi.org/10.5194/acp-6-3181-2006, 2006.

Guo, H., So, K. L., Simpson, I. J., Barletta, B., Meinardi, S., and Blake, D. R.: C_1–C_8 volatile organic compounds in the atmosphere of Hong Kong: Overview of atmospheric processing and source apportionment, Atmos. Environ., 41, 1456–1472, 2007.

Guo, H., Jiang, F., Cheng, H. R., Simpson, I. J., Wang, X. M., Ding, A. J., Wang, T. J., Saunders, S. M., Wang, T., Lam, S. H. M., Blake, D. R., Zhang, Y. L., and Xie, M.: Concurrent observations of air pollutants at two sites in the Pearl River Delta and the implication of regional transport, Atmos. Chem. Phys., 9, 7343–7360, https://doi.org/10.5194/acp-9-7343-2009, 2009.

Guo, H., Ling, Z. H., Cheung, K., Jiang, F., Wang, D. W., Simpson, I. J., Barletta, B., Meinardi, S., Wang, T. J., Wang, X. M., Saunders, S. M., and Blake, D. R.: Characterization of photochemical pollution at different elevations in mountainous areas in Hong Kong, Atmos. Chem. Phys., 13, 3881–3898, https://doi.org/10.5194/acp-13-3881-2013, 2013.

He, K.: Multi-resolution Emission Inventory for China (MEIC): model framework and 1990–2010 anthropogenic emissions, in: AGU Fall Meeting Abstracts, A32B-05, December 2012.

HKEPD: Air Quality in Hong Kong 2014, available at: http://www.aqhi.gov.hk/api_history/english/report/files/AQR2014e_Update0616.pdf (last access: 26 March 2018), Hong Kong Environmental Protection Department, 2015.

Huang, J. P., Fung, J. C. H., Lau, A. K. H., and Qin, Y.: Numerical simulation and process analysis of typhoon-related ozone episodes in Hong Kong, J. Geophys. Res., 110, D05301, https://doi.org/10.1029/2004jd004914, 2005.

Huang, J. P., Fung, J. C., and Lau, A. K.: Integrated processes analysis and systematic meteorological classification of ozone episodes in Hong Kong, J. Geophys. Res.-Atmos., 111, D20309, https://doi.org/10.1029/2005JD007012, 2006.

IPCC: Climate Change 2014: Synthesis Report. Contribution of Working Groups I, II and III to the Fifth Assessment Report of the Intergovernmental Panel on Climate Change, edited by: Core Writing Team, Pachauri, R. K., and Meyer, L. A., IPCC, Geneva, Switzerland, 151, 2014.

Jenkin, M. E., Saunders, S. M., and Pilling, M. J.: The tropospheric degradation of volatile organic compounds: A protocol for mechanism development, Atmos. Environ., 31, 81–104, 1997.

Jenkin, M. E., Saunders, S. M., Wagner, V., and Pilling, M. J.: Protocol for the development of the Master Chemical Mechanism, MCM v3 (Part B): tropospheric degradation of aromatic volatile organic compounds, Atmos. Chem. Phys., 3, 181–193, https://doi.org/10.5194/acp-3-181-2003, 2003.

Jiang, F., Wang, T., Wang, T., Xie, M., and Zhao, H.: Numerical modeling of a continuous photochemical pollution episode in Hong Kong using WRF–chem, Atmos. Environ., 42, 8717–8727, 2008.

Jiang, F., Guo, H., Wang, T., Cheng, H., Wang, X., Simpson, I., Ding, A., Saunders, S., Lam, S., and Blake, D.: An ozone episode in the Pearl River Delta: Field observation and model simulation, J. Geophys. Res., 115, D22305, https://doi.org/10.1029/2009JD013583, 2010.

Jiang, Y. C., Zhao, T. L., Liu, J., Xu, X. D., Tan, C. H., Cheng, X. H., Bi, X. Y., Gan, J. B., You, J. F., and Zhao, S. Z.: Why does surface ozone peak before a typhoon landing in southeast China?, Atmos. Chem. Phys., 15, 13331–13338, https://doi.org/10.5194/acp-15-13331-2015, 2015.

Kleffmann, J.: Daytime sources of nitrous acid (HONO) in the atmospheric boundary layer, Chemistry and Physical Chemistry, 8, 1137–1144, 2007.

Kumar, P. and Imam, B.: Footprints of air pollution and changing environment on the sustainability of built infrastructure, Sci. Total Environ., 444, 85–101, https://doi.org/10.1016/j.scitotenv.2012.11.056, 2013.

Kurokawa, J., Ohara, T., Morikawa, T., Hanayama, S., Janssens-Maenhout, G., Fukui, T., Kawashima, K., and Akimoto, H.: Emissions of air pollutants and greenhouse gases over Asian regions during 2000–2008: Regional Emission inventory in ASia (REAS) version 2, Atmos. Chem. Phys., 13, 11019–11058, https://doi.org/10.5194/acp-13-11019-2013, 2013.

Lam, S. H. M., Saunders, S. M., Guo, H., Ling, Z. H., Jiang, F., Wang, X. M., and Wang, T. J.: Modelling VOC source impacts on high ozone episode days observed at a mountain summit in Hong Kong under the influence of mountain-valley breezes, Atmos. Environ., 81, 166–176, https://doi.org/10.1016/j.atmosenv.2013.08.060, 2013.

Lefohn, A. S., Shadwick, D., and Oltmans, S. J.: Characterizing changes in surface ozone levels in metropolitan and rural areas in the United States for 1980–2008 and 1994–2008, Atmos. Environ., 44, 5199–5210, 2010.

Li, J. F., Lu, K. D., Lv, W., Li, J., Zhong, L. J., Ou, Y. B., Chen, D. H., Huang, X., and Zhang, Y. H.: Fast increasing of surface ozone concentrations in Pearl River Delta characterized by a regional air quality monitoring network during 2006–2011, J. Environ. Sci.-China, 26, 23–36, 2014.

Li, Z. Y., Xue, L. K., Yang, X., Zha, Q. Z., Tham, Y. J., Yan, C., Louie, P. K. K., Luk, C. W. Y., Wang, T., and Wang, W. X.: Oxidizing capacity of the rural atmosphere in Hong Kong, Southern China, Sci. Total Environ., 612, 1114–1122, https://doi.org/10.1016/j.scitotenv.2017.08.310, 2018.

Lin, M., Horowitz, L. W., Payton, R., Fiore, A. M., and Tonnesen, G.: US surface ozone trends and extremes from 1980 to 2014: quantifying the roles of rising Asian emissions, domestic controls, wildfires, and climate, Atmos. Chem. Phys., 17, 2943–2970, https://doi.org/10.5194/acp-17-2943-2017, 2017.

Ling, Z. H., Guo, H., Zheng, J. Y., Louie, P. K. K., Cheng, H. R., Jiang, F., Cheung, K., Wong, L. C., and Feng, X. Q.: Establishing a conceptual model for photochemical ozone pollution in subtropical Hong Kong, Atmos. Environ., 76, 208–220, https://doi.org/10.1016/j.atmosenv.2012.09.051, 2013.

Ling, Z. H., Guo, H., Lam, S., Saunders, S., and Wang, T.: Atmospheric photochemical reactivity and ozone production at two sites in Hong Kong: Application of a Master Chemical Mechanism–photochemical box model, J. Geophys. Res.-Atmos., 119, 10567–10582, 2014.

Liu, H. and Chan, J. C. L.: An investigation of air-pollutant patterns under sea–land breezes during a severe air-pollution episode in Hong Kong, Atmos. Environ., 36, 591–601, 2002.

Liu, K.-Y., Wang, Z., and Hsiao, L.-F.: A modeling of the sea breeze and its impacts on ozone distribution in northern Taiwan, Environ. Modell. Softw., 17, 21–27, 2002.

Lo, J. C. F., Lau, A. K. H., Fung, J. C. H., and Chen, F.: Investigation of enhanced cross-city transport and trapping of air pollutants by coastal and urban land-sea breeze circulations, J. Geophys. Res.-Atmos., 111, D14104, https://doi.org/10.1029/2005JD006837, 2006.

Lu, X., Chow, K. C., Yao, T., Fung, J. C. H., and Lau, A. K. H.: Seasonal variation of the land-sea breeze circulation in the Pearl River Delta region, J. Geophys. Res.-Atmos., 114, D17112, https://doi.org/10.1029/2009JD011764, 2009.

Lu, X., Chow, K.-C., Yao, T., Lau, A. K. H., and Fung, J. C. H.: Effects of urbanization on the land sea breeze circulation over the Pearl River Delta region in winter, Int. J. Climatol., 1089–1104, https://doi.org/10.1002/joc.1947, 2010.

Monks, P. S., Archibald, A. T., Colette, A., Cooper, O., Coyle, M., Derwent, R., Fowler, D., Granier, C., Law, K. S., Mills, G. E., Stevenson, D. S., Tarasova, O., Thouret, V., von Schneidemesser, E., Sommariva, R., Wild, O., and Williams, M. L.: Tropospheric ozone and its precursors from the urban to the global scale from air quality to short-lived climate forcer, Atmos. Chem. Phys., 15, 8889–8973, https://doi.org/10.5194/acp-15-8889-2015, 2015.

NARSTO: An Assessment of Tropospheric Ozone Pollution-A North American Perspective, NARSTO Management Office (Envair), Pasco, Washington, 2000.

NRC: Rethinking the Ozone Problem in Urban and Regional Air Pollution, National Research Council, Washington, D.C., 1991.

Parrish, D. D., Trainer, M., Holloway, J. S., Yee, J. E., Warshawsky, M. S., Fehsenfeld, F. C., Forbes, G. L., and Moody, J. L.: Relationships between ozone and carbon monoxide at surface sites in the North Atlantic region, J. Geophys. Res.-Atmos., 103, 13357–13376, 1998.

Parrish, D. D., Law, K. S., Staehelin, J., Derwent, R., Cooper, O. R., Tanimoto, H., Volz-Thomas, A., Gilge, S., Scheel, H.-E., Steinbacher, M., and Chan, E.: Long-term changes in lower tropospheric baseline ozone concentrations at northern mid-latitudes, Atmos. Chem. Phys., 12, 11485–11504, https://doi.org/10.5194/acp-12-11485-2012, 2012.

Ran, L., Zhao, C. S., Xu, W. Y., Lu, X. Q., Han, M., Lin, W. L., Yan, P., Xu, X. B., Deng, Z. Z., Ma, N., Liu, P. F., Yu, J., Liang, W. D., and Chen, L. L.: VOC reactivity and its effect on ozone production during the HaChi summer campaign, Atmos. Chem. Phys., 11, 4657–4667, https://doi.org/10.5194/acp-11-4657-2011, 2011.

Saunders, S. M., Jenkin, M. E., Derwent, R. G., and Pilling, M. J.: Protocol for the development of the Master Chemical Mechanism, MCM v3 (Part A): tropospheric degradation of non-aromatic volatile organic compounds, Atmos. Chem. Phys., 3, 161–180, https://doi.org/10.5194/acp-3-161-2003, 2003.

Seinfeld, J. H. and Pandis, S. N.: Atmospheric chemistry and physics: from air pollution to climate change, John Wiley & Sons, 2016.

Shindell, D., Kuylenstierna, J. C. I., Vignati, E., van Dingenen, R., Amann, M., Klimont, Z., Anenberg, S. C., Muller, N., Janssens-Maenhout, G., Raes, F., Schwartz, J., Faluvegi, G.,

Pozzoli, L., Kupiainen, K., Hoglund-Isaksson, L., Emberson, L., Streets, D., Ramanathan, V., Hicks, K., Oanh, N. T. K., Milly, G., Williams, M., Demkine, V., and Fowler, D.: Simultaneously Mitigating Near-Term Climate Change and Improving Human Health and Food Security, Science, 335, 183–189, https://doi.org/10.1126/science.1210026, 2012.

Simpson, I. J., Blake, N. J., Barletta, B., Diskin, G. S., Fuelberg, H. E., Gorham, K., Huey, L. G., Meinardi, S., Rowland, F. S., Vay, S. A., Weinheimer, A. J., Yang, M., and Blake, D. R.: Characterization of trace gases measured over Alberta oil sands mining operations: 76 speciated C_2–C_{10} volatile organic compounds (VOCs), CO_2, CH_4, CO, NO, NO_2, NO_y, O_3 and SO_2, Atmos. Chem. Phys., 10, 11931–11954, https://doi.org/10.5194/acp-10-11931-2010, 2010.

Skamarock, W. C., Klemp, J. B., Dudhia, J., Gill, D. O., Barker, D. M., Duda, M. G., Huang, X.-Y., Wang, W., and Powers, J. G.: A Description of the Advanced Research WRF Version 3, NCAR Tech. Note NCAR/TN-475+STR, 113 pp., https://doi.org/10.5065/D68S4MVH, 2008.

Stein, A. F., Draxler, R. R., Rolph, G. D., Stunder, B. J. B., Cohen, M. D., and Ngan, F.: NOAA's HYSPLIT atmospheric transport and dispersion modeling system, B. Am. Meteorol. Soc., 96, 2059–2077, 2015.

Sun, L., Xue, L., Wang, T., Gao, J., Ding, A., Cooper, O. R., Lin, M., Xu, P., Wang, Z., Wang, X., Wen, L., Zhu, Y., Chen, T., Yang, L., Wang, Y., Chen, J., and Wang, W.: Significant increase of summertime ozone at Mount Tai in Central Eastern China, Atmos. Chem. Phys., 16, 10637–10650, https://doi.org/10.5194/acp-16-10637-2016, 2016.

Velchev, K., Cavalli, F., Hjorth, J., Marmer, E., Vignati, E., Dentener, F., and Raes, F.: Ozone over the Western Mediterranean Sea – results from two years of shipborne measurements, Atmos. Chem. Phys., 11, 675–688, https://doi.org/10.5194/acp-11-675-2011, 2011.

Wang, N., Guo, H., Jiang, F., Ling, Z. H., and Wang, T.: Simulation of ozone formation at different elevations in mountainous area of Hong Kong using WRF-CMAQ model, Sci. Total Environ., 505, 939–951, 2015.

Wang, T., LAM, K. S., and LEE, A. S. Y.: Meteorological and Chemical Characteristics of the Photochemical Ozone Episodes Observed at Cape D'Aguilar in Hong Kong, J. Appl. Meteorol., 30, 1167–1178, 1998.

Wang, T., Guo, H., Blake, D. R., Kwok, Y. H., Simpson, I. J., and Li, Y. S.: Measurements of Trace Gases in the Inflow of South China Sea Background Air and Outflow of Regional Pollution at Tai O, Southern China, J. Atmos. Chem., 52, 295–317, https://doi.org/10.1007/s10874-005-2219-x, 2005.

Wang, T., Wei, X. L., Ding, A. J., Poon, C. N., Lam, K. S., Li, Y. S., Chan, L. Y., and Anson, M.: Increasing surface ozone concentrations in the background atmosphere of Southern China, 1994–2007, Atmos. Chem. Phys., 9, 6217–6227, https://doi.org/10.5194/acp-9-6217-2009, 2009.

Wang, Y., Wang, H., Guo, H., Lyu, X., Cheng, H., Ling, Z., Louie, P. K. K., Simpson, I. J., Meinardi, S., and Blake, D. R.: Long-term O_3-precursor relationships in Hong Kong: field observation and model simulation, Atmos. Chem. Phys., 17, 10919–10935, https://doi.org/10.5194/acp-17-10919-2017, 2017.

Wang, Y., Guo, H., Zou, S., Lyu, X., Wang, H., Ling, Z., and Cheng, H.: Ground level O_3 photochemistry over

South China Sea: Application of a near-explicit chemical mechanism box model, Environ. Pollut., 234, 155–166, https://doi.org/10.1016/j.envpol.2017.11.001, 2018.

Wei, X., Lam, K.-S., Cao, C., Li, H., and He, J.: Dynamics of the Typhoon Haitang Related High Ozone Episode over Hong Kong, Adv. Meteorol., 2016, 1–12, https://doi.org/10.1155/2016/6089154, 2016.

WHO: Health aspects of air pollution with particulate matter, ozone and nitrogen dioxide: report on a WHO working group, Bonn, Germany 13–15 January 2003, World Health Organization, 2003.

Willmott, C. J.: Some comments on the evaluation of model performance, B. Am. Meteorol. Soc., 63, 1309–1313, 1982.

Xu, X., Lin, W., Wang, T., Yan, P., Tang, J., Meng, Z., and Wang, Y.: Long-term trend of surface ozone at a regional background station in eastern China 1991–2006: enhanced variability, Atmos. Chem. Phys., 8, 2595–2607, https://doi.org/10.5194/acp-8-2595-2008, 2008.

Xu, Z., Wang, T., Wu, J., Xue, L., Chan, J., Zha, Q., Zhou, S., Louie, P. K. K., and Luk, C. W.: Nitrous acid (HONO) in a polluted subtropical atmosphere: Seasonal variability, direct vehicle emissions and heterogeneous production at ground surface, Atmos. Environ., 106, 100–109, 2015.

Xue, L. K., Wang, T., Louie, P. K. K., Luk, C. W. Y., Blake, D. R., and Xu, Z.: Increasing External Effects Negate Local Efforts to Control Ozone Air Pollution: A Case Study of Hong Kong and Implications for Other Chinese Cities, Environ. Sci. Technol., 48, 10769–10775, https://doi.org/10.1021/es503278g, 2014.

Xue, L., Gu, R., Wang, T., Wang, X., Saunders, S., Blake, D., Louie, P. K. K., Luk, C. W. Y., Simpson, I., Xu, Z., Wang, Z., Gao, Y., Lee, S., Mellouki, A., and Wang, W.: Oxidative capacity and radical chemistry in the polluted atmosphere of Hong Kong and Pearl River Delta region: analysis of a severe photochemical smog episode, Atmos. Chem. Phys., 16, 9891–9903, https://doi.org/10.5194/acp-16-9891-2016, 2016.

Yang, J. X., Lau, A. K. H., Fung, J. C. H., Zhou, W., and Wenig, M.: An air pollution episode and its formation mechanism during the tropical cyclone Nuri's landfall in a coastal city of south China, Atmos. Environ., 54, 746–753, https://doi.org/10.1016/j.atmosenv.2011.12.023, 2012.

Yin, L. H.: Analysis of Meteorological Criteria Leading to Tropical Cyclone Related Ozone Episodes in Hong Kong, PhD, HKUST, 2004.

Zha, Q.: Measurement of nitrous acid (HONO) and the implications to photochemical pollution, MPhil dissertation, The Hong Kong Polytechnic University, 2015.

Zhang, M. and Zhang, L.: Study of the sea-land breeze system in Hong Kong, Hong Kong Meteorological Society Bulletin, 7, 22–42, 1997.

Zhang, Q., Yuan, B., Shao, M., Wang, X., Lu, S., Lu, K., Wang, M., Chen, L., Chang, C.-C., and Liu, S. C.: Variations of ground-level O_3 and its precursors in Beijing in summertime between 2005 and 2011, Atmos. Chem. Phys., 14, 6089–6101, https://doi.org/10.5194/acp-14-6089-2014, 2014.

Zheng, J. Y., Zhong, L. J., Wang, T., Louie, P. K. K., and Li, Z. C.: Ground-level ozone in the Pearl River Delta region: Analysis of data from a recently established regional air quality monitoring network, Atmos. Environ., 44, 814–823, 2010.